




OPEN

Adsorption of Cr(VI), Ni(II), Fe(II) and Cd(II) ions by KIAgNPs decorated MWCNTs in a batch and fixed bed process

Titus Chinedu Egbosiuba^{1,2,6}, Ambali Saka Abdulkareem^{1,6}, Abdulsalami Sanni Kovo^{1,6}, Eytayo Amos Afolabi¹, Jimoh Oladejo Tijani^{3,6}, Mercy Temitope Bankole^{3,6}, Shufeng Bo⁴ & Wiets Daniel Roos⁵

The efficient removal of toxic metals ions from chemical industry wastewater is considered problematic due to the existence of pollutants as mixtures in the aqueous matrix, thus development of advanced and effective treatment method has been identified as a panacea to the lingering problems of heavy metal pollution. In this study, KIAgNPs decorated MWCNTs nano adsorbent was developed using combination of green chemistry protocol and chemical vapor deposition techniques and subsequently characterized using UV-Vis, HRTEM, HRSEM, XRD, FTIR and XPS. The adsorptive efficiency of MWCNTs-KIAgNPs for the removal of Cr(VI), Ni(II), Fe(II), Cd(II) and physico-chemical parameters like pH, TDS, COD, BOD, nitrates, sulphates, chlorides and phosphates from chemical industrial wastewater was examined in both batch and fixed bed systems. The result exhibited successful deposition of KIAgNPs on the surface of MWCNTs as confirmed by the microstructures, morphology, crystalline nature, functional groups and elemental characteristics of the MWCNTs-KIAgNPs. Optimum batch adsorption parameters include; pH (3 for Cr(VI) and 6 for Ni(II), Fe(II) and Cd(II) ions), contact time (60 min), adsorbent dosage (40 mg) and temperature (318 K). The binding capacities were obtained as follows; Cr⁶⁺ (229.540 mg/g), Ni²⁺ (174.784 mg/g), Fe²⁺ (149.552) and Cd²⁺ (121.026 mg/g), respectively. Langmuir isotherm and pseudo-second order kinetic model best described the experimental data in batch adsorption, while the thermodynamic parameters validated the chemisorption and endothermic nature of the adsorption process. In continuous adsorption, the metal ions were effectively removed at low metal influent concentration, low flow rate and high bed depth, whereby the experimental data were designated by Thomas model. The high physico-chemical parameters in the wastewater were successfully treated in both batch and fixed bed systems to fall within WHO permissible concentrations. The adsorption/desorption study illustrated over 80% metal removal by MWCNTs-KIAgNPs even after 8th adsorption cycle. This study demonstrated excellent performance of MWCNTs-KIAgNPs for chemical industry wastewater treatment.

Wastewater is a major public health problem which are generated from chemical industries such as battery, metal plating, cosmetics, pharmaceuticals, plastic and textiles¹⁻³. The wastewater contains various pollutants, including potentially toxic metals which are detrimental to humans, animals and aquatic organisms. Heavy metals such as Cd(II), Cr(VI) Fe(II) and Ni(II) are increasingly recognized as a serious global threat to public health due to their non-biodegradability, mobility, toxicity and bioaccumulation potentials in the liver, kidney and other human bodies^{4,5}. For instance, chronic exposure to cadmium have adverse impact on human bone, kidney, increases blood pressure and causes cancer⁶. An increase in exposure to chromium results to cancer, asthma, diarrhea. Liver defect, kidney problems and brain defect leading to physiological impairment^{7,8}. The presence

¹Department of Chemical Engineering, Federal University of Technology, PMB.65, Minna, Niger, Nigeria. ²Department of Chemical Engineering, Chukwuemeka Odumegwu Ojukwu University, PMB 02, Uli, Anambra, Nigeria. ³Department of Chemistry, Federal University of Technology, PMB.65, Minna, Niger, Nigeria. ⁴Faculty of Light Industry and Chemical Engineering, Dalian Polytechnic University, Dalian 116034, People's Republic of China. ⁵Department of Physics, University of the Free State, P.O. Box 339, Bloemfontein 9300, South Africa. ⁶Nanotechnology Research Group, Africa Centre of Excellence for Mycotoxin and Food Safety, Federal University of Technology, P.M.B 65, Bosso, Minna, Niger, Nigeria. email: egbosiubachinedu@gmail.com

of iron above tolerable limit in wastewater have been reported to be carcinogenic and causes intestinal damage and irritation of respiratory tract⁹. While long term exposure to nickel is also carcinogenic and a major cause of brain hemorrhage, cardiac arrest, asthma, dermatitis, liver and heart damage¹⁰. Therefore, the primary concern of wastewater treatment experts is to mitigate the presence of these heavy metals in aqueous matrix even in trace amounts. Recent developments on the non-degradability and toxicity of these heavy metals have heightened the interests in the removal of these heavy metals from industrial wastewater⁴.

Recently, researchers have examined the removal of heavy metals using numerous techniques, including ion exchange, chemical precipitation, reverse osmosis, membrane processes, microbial biotechnology, coagulation, flocculation, filtration and adsorption technology¹¹. However, these techniques possess different limitations such as low efficiency, high cost, generation of toxic byproducts, delay in operation, inefficiency in targeting specific pollutants and complexity of treatment methods¹². Of these techniques, adsorption technology has been identified as one of the most efficient and commonly used treatment method due to its ease of operation control, regeneration potentials, cost efficient, inertness to materials, lack of sludge formation and variety of adsorbents^{13–15}. In recent years, nanomaterials have attracted the attention of researchers due to their unique physicochemical properties attributable to their small size, shape, dimensions, large surface area, crystallinity and composition¹⁶. These foremost properties enhanced the suitability of nanomaterials application in water treatment, catalysis, medicine and biotechnology¹². At the moment, nanomaterials-based adsorbents such as zinc oxide, tin oxide, graphene oxide, carbon nanotubes, silica, aluminum oxide, titanium oxide, zeolites, iron oxide, spinel ferrites, chitosan, carbon nanofibers and cerium oxide have been employed by different researchers for industrial wastewater treatment^{17–25}. Among these nanomaterials, carbon nanotubes (CNTs) have been extensively exploited due to their large surface area, ease of modification, extraordinary surface chemistry, structural control, low density, porosity, higher thermal stability, high chemical stability, regeneration ease and reusability, compared to other adsorbents²⁶. Previous studies have reported increase in the adsorption capacity of CNTs in the uptake of heavy metals from wastewater after oxidation with either acid or base²³. Similarly, the successful interaction of the oxidized CNTs with the heavy metals and even organic compounds have been attributed to their surface functional groups and hydrophobic surfaces through electrostatic and hydrogen bonding²².

In view of the interaction of the surface chemistry of CNTs, some studies have investigated the incorporation of metallic nanoparticles to the surface of CNTs due to their distinctive properties such as antimicrobial activities, catalysis, electricity conduction and high stability for chemicals²⁷. Metal nanoparticles such as copper (Cu), iron (Fe), cobalt (Co), nickel (Ni), palladium (Pd), gold (Au), platinum (Pt) and silver (Ag) are frequently used^{28,29}. Among the metallic nanoparticles (NPs), AgNPs are the most widely utilized in the removal of heavy metals, organic matters, dyes and antibiotics from wastewater. AgNPs have been synthesized through different chemical and physical methods which are not eco-friendly due to hazardous chemical utilization, expensive and operated at high temperature. Recent evidence suggests that efforts to mitigate the increased environmental challenges of the chemical techniques enhanced the development of green synthesis of AgNPs using plant materials, fungi, algae and bacteria³⁰. Of these, plant extracts have been dominantly utilized because of its low cost, less toxicity, improved structural control and lack of pre-treatment methods²⁸. The plant extracts contain various phytochemicals such as flavonoids and polyphenolic substances which facilitates the reduction of silver salt to zerovalent silver NPs and also protects it from agglomeration. Similarly, plant extracts and plant derivatives such as *Koelreuteria apiculata*³⁰, starch solution¹², *Nauclea latifolia*³¹ and *Diospyros lotus*³² have been used to synthesize AgNPs via green chemistry. To the best of our knowledge, no study has reported the green synthesis of AgNPs using *Khaya ivorensis* (African mahogany) leaf extract.

In the current study, *Khaya ivorensis* (KI) plant extract was utilized to synthesize KIAgNPs for the decoration of MWCNTs. The developed MWCNTs-KIAgNPs were characterized and the efficiency of MWCNTs-KIAgNPs for the adsorption of Cd(II), Cr(VI), Fe(II) and Ni(II) from industrial wastewater was investigated in a batch and dynamic flow processes. Overall, continuous column adsorption is the most favorable system for potential practical applications of developed adsorbent in wastewater treatment. In spite of the fixed bed column adsorption significance, there is paucity of information on the removal of Cd(II), Cr(VI), Fe(II) and Ni(II) using MWCNTs-KIAgNPs. The influence of pH, adsorbent dosage, temperature and contact time on the metal adsorption were explored for the batch mode, while the influent concentration, flow rate and bed depth were examined for the continuous flow adsorption.

Materials and methods

Materials. Sodium hydroxide (NaOH), Silver nitrate (AgNO₃, 99.9%), dimethylformamide (DMF, 99%) and hydrochloric acid (HCl, 99%) of analytical grade were purchased from Sigma Aldrich and used as received without further purification. Deionized water obtained by Milli-Q system was used throughout the research. Healthy leaves of *Khaya ivorensis* (KI) were collected from Bosso campus of Federal University of Technology Minna, Nigeria. The identification and authentication of the plant was properly done prior to deposition of the sample in the university herbarium with the sample number FUT/STEP-B/T005. The wastewater was collected from the clusters of chemical industries at industrial layout Nnewi, Anambra Nigeria. The MWCNTs used in this study were synthesized as reported in our previous study³³.

Preparation of KI leaf extract. To prepare the plant extract, KI leaves were washed with distilled water followed by deionized water. 100 g of the KI leaves were cut into small pieces and boiled with 1000 mL of deionised water at 60 °C for 30 min to obtain aqueous extract. Thereafter, the KI extract was cooled, filtered by Whatman No. 1 filter paper and stored at 40 °C for further application in biosynthesis of KIAgNPs.

Phytochemical analysis. Herein, main secondary metabolites in plant extract that enhances the formation of nanoparticles were identified by determining the presence of phytochemicals like tannins, phenols, alkaloids, saponins, flavonoids, steroids and terpenoids. Initially, the presence of tannins was confirmed by the appearance of greenish black or dark blue as 2 mL of 5% ferric chloride was added to 1 mL of KI extract³⁴. Phenols were identified by the addition of 2 mL of 5% ferric chloride into 0.2 g of the plant extract and the formation of a greenish-brown or black precipitate color indicate presence for phenols³². Also, alkaloids presence in the KI extract was revealed if a white or green precipitate appears on addition of few drops of Mayer's reagent into a mixture containing 2 mL each of the KI extract and dilute hydrochloric acid³². In order to determine the presence of saponins, about 0.2 g of KI leaves were added to 5 mL of distilled water, shaken for some time and heated to boil. Then saponins were confirmed to be present with a stable foam (froth) appearance³⁵. The flavonoids were examined by treating the KI extract (1 mL) with 10% NaOH solution (1 mL), while the appearance of intense yellow precipitate confirmed the presence of flavonoids³⁴. About 0.5 g of dried KI extract was dissolved in 2 mL of acetic anhydride solution before adding concentrated sulfuric acid (2 mL), then the occurrence of steroids was confirmed with color change from violet to green or blue³². The determination of terpenoids was achieved by mixing dried extract (0.1 g) with chloroform (0.5 mL) prior to careful introduction of concentrated sulfuric acid (1 mL) to form a layer. The presence of a reddish brown color at the interface confirmed the formation of terpenoids³⁵.

Subsequently, the quantification of the total tannins, phenols, alkaloids and flavonoids in the aqueous KI leaf extract were determined through validated methods and standard procedures^{32,34–36}.

Optimization of green synthesis of KIAgNPs. In this study, the influence of various parameters such as temperature, pH and volume of KI extract to silver nitrate solution were investigated using factorial design of experiment shown in Table 2a for high and low values of the parameters. Notably, green synthesis of KIAgNPs was carried out in a dark room using an ultrasonic bath (SB25-12DT, Ultrasonic Scientz). As shown in Table 2b, 80 mL of KI extract and 20 mL of silver nitrate (0.05 M) solution was measured into a 250 cm³ conical flask maintained at the pH of 8 (using HCl and NaOH) and placed inside the ultrasonic bath set at 70 °C. As the temperature was achieved, the KI extract was added to the AgNO₃ solution with the heating maintained for 15 min. Thereafter, the reduction of silver ions (Ag⁺) to silver (Ag⁰) nanoparticles was observed through color change from yellow to deep brown³⁷. Also, the wavelength of the sample was determined using UV-visible spectroscopy and the same procedure was repeated for runs 2 to 8 as indicated in Table 2b.

Decoration of MWCNTs with KIAgNPs. In this study, MWCNTs-KIAgNPs composite were prepared in two phases to incorporate carboxyl and hydroxyl functional groups and to enhance the adsorption properties of MWCNTs with KIAgNPs.

Herein, MWCNTs-KIAgNPs composite were prepared in two phases to incorporate carboxyl and hydroxyl functional groups and to enhance the adsorption properties of MWCNTs with KIAgNPs. In the first phase of the nano adsorbent fabrication, 25 g of MWCNTs was mixed with 200 and 600 mL of nitric acid and sulfuric acid in order to incorporate negatively charged functional groups to the MWCNTs surface³⁸. Thereafter, the mixture was placed in ultrasonic bath set at 40 °C for 3 h to add carboxyl and hydroxyl groups onto the surface of MWCNTs. Subsequently, the mixture was washed with deionized water to a neutral pH and filtered using Whatman grade 1 filter paper. In the end, the functionalized MWCNTs was oven dried at 110 °C for 12 h.

Furthermore, the second phase is the enhancement of the properties of functionalized MWCNTs using KIAgNPs. Herein, 20 g of the MWCNTs was dispersed in a solution containing 50 mL of DMF and 100 mL KIAgNPs and sonicated for 3 h to enhance the dispersion of the carbon nanotubes with the homogenous blend of the silver nanoparticles. Thereafter, the blend of MWCNTs-KIAgNPs was washed with distilled water until a neutral pH was achieved for the washed water. Subsequently, the obtained MWCNTs-KIAgNPs was oven dried at 110 °C for 12 h. Following this, the MWCNTs-KIAgNPs hybrid was stored in an airtight container for further characterization and used as nano adsorbent for the uptake of Cd(II), Cr(VI), Fe(II) and Ni(II) from chemical industrial wastewater in a batch and fixed bed process.

Characterization of KIAgNPs and MWCNTs-KIAgNPs. The formation and optimization of KIAgNPs were studied using a UV-visible spectroscopy (Cary100, Agilent Technologies, USA). The KIAgNPs and MWCNTs-KIAgNPs were characterized for their microstructures using high resolution transmission electron microscope (HRTEM, Zeiss Auriga). The morphological analysis of MWCNTs-KIAgNPs was examined by high resolution scanning electron microscopy (HRSEM, Zeiss Auriga). The MWCNTs-KIAgNPs surface area was examined using Brunauer-Emmett-Teller (NOVA4200e, Quantachrome UK), while their phase structures were analyzed using X-ray diffraction (XRD, 6000, Shimadzu Scientific). Additionally, the measurement of the zeta potential was carried out using a zetaView PMX100 micro-electrophoretic instrument (Particle Metrix GmbH, Meerbusch, Germany). The point of zero charge (PZC) was determined by titration method, where MWCNTs-KIAgNPs of 0.04 g were added to deionized water. The pH meter (Eutech Instruments) was utilized for solutions charge densities determination, while the 0.05 M of HNO₃ and NaOH was used to adjust the surface charge of MWCNTs-KIAgNPs in the pH range of 2–8 until a zero charge density was obtained.

Adsorption performance evaluation. *Metal analysis and physicochemical characterization.* Herein, the presence of metal ions such as Cr(VI), Ni(II), Fe(II) and Cd(II) in the chemical industry wastewater were evaluated using atomic absorption spectrometer (AAS, PG 900 Instruments, UK) method after proper dilution. Standard techniques were particularly used for physicochemical analysis of the wastewater before and after treatment in a batch and dynamic column mode. The pH, total dissolved solids (TDS), chemical oxygen demand

(COD) and biochemical oxygen demand (BOD) were determined by pH meter, gravimetric procedure, 5 days technique and filtrate drying technique^{39,40}. Further, the nitrates, sulphates, chlorides and phosphates were determined by brucine reagent, gum acacia, argentometric titration and ammonium molybdate reagent^{40,41}.

Batch adsorption studies. Batch adsorption parameters such as pH, contact time, amount of MWCNTs-KIAG-NPs and temperature were duly optimized to enable improved removal of Cd(II), Cr(VI), Fe(II) and Ni(II) from chemical industrial wastewater. In this study, the influence of adsorption parameters on metal ions removal were varied as follows; pH (2 to 8, altered using 0.1 mol/L NaOH or HNO₃), contact time (10 to 120 min), amount of MWCNTs-KIAG-NPs (10 to 60 mg) and temperature (303 to 318 K). Initially, 10 mg of MWCNTs-KIAG-NPs was added to 100 mL of wastewater solution containing 44, 85, 56 and 66 mg/L of Cd(II), Cr(VI), Fe(II) and Ni(II) in a sealed conical flask (200 mL) and stirred continuously (150 rpm) in a thermostatic bath for 10 min at a pH and temperature of 5 and 40 °C, respectively. Thereafter, the sample was filtered using Whatman grade 1 filter paper and the filtrate analyzed for the remaining adsorbate amount by atomic adsorption spectrophotometer (AAS, PG 990, PG Instruments, UK). Similarly, the optimized process parameters were achieved using the same procedure to investigate the adsorption conditions on the removal rate of Cd(II), Cr(VI), Fe(II) and Ni(II) ions by MWCNTs-KIAG-NPs.

The rate of removal (R) and the adsorption capacity (q_t and q_e (mg/g)) were evaluated using the following mathematical expressions^{42,43}.

$$R = \frac{C_0 - C_{e,t}}{C_0} \times 100\% \quad (1)$$

$$q_t = \frac{(C_0 - C_t)V}{m} \quad (2)$$

$$q_e = \frac{(C_0 - C_e)V}{m} \quad (3)$$

in which q_t and q_e refers to the adsorption capacity of metal ions at t (min) and equilibrium time, respectively. C₀ (mg/L) is the initial concentration, while C_e (mg/L) and C_t (mg/L) denotes the equilibrium and t time concentration of metal ions, respectively. Also, m (mg) and V (L) are the amount of adsorbent and volume of adsorbate solution.

Further evaluation of the static adsorption behavior of Cd(II), Cr(VI), Fe(II) and Ni(II) ions by MWCNTs-KIAG-NPs was conducted using Langmuir⁴⁴ and Freundlich¹⁰ adsorption isotherm models described in Eqs. (4) and (5), respectively.

$$\frac{C_e}{q_e} = \frac{1}{K_L q_m} + \frac{C_e}{q_m} \quad (4)$$

$$\ln q_e = \ln K_F + \frac{1}{n_F} \ln C_e \quad (5)$$

in which the maximum adsorption capacity and Langmuir coefficient are denoted by q_m (mg/g) and K_L (L/mg). Also, K_F is the Freundlich equilibrium constant, representing the degree of the adsorption capacity, while n_F is the heterogeneity factor that measures the strength of adsorption.

In addition, pseudo first-order and pseudo second-order models were utilized to fit the kinetic data using the relationships expressed in Eqs. (6) and (7)⁴², respectively.

$$\ln(q_e - q_t) = \ln q_e - k_1 t \quad (6)$$

$$\frac{t}{q_t} = \frac{1}{k_2 q_e^2} + \frac{t}{q_e} \quad (7)$$

in which k₁ (min⁻¹) and k₂ (g/mg min) represent the rate constants for the pseudo-first-order and pseudo-second-order kinetic model.

Also, thermodynamic parameters for instance; Gibbs free energy (ΔG°), enthalpy (ΔH°) and entropy (ΔS°) were evaluated to establish the nature of Cd(II), Cr(VI), Fe(II) and Ni(II) ions capture by MWCNTs-KIAG-NPs using Eqs. (8) and (9)⁴⁵.

$$\Delta G^\circ = \Delta H^\circ - T \Delta S^\circ \quad (8)$$

$$\ln \frac{q_e}{C_e} = -\frac{\Delta H^\circ}{RT} + \frac{\Delta S^\circ}{R} \quad (9)$$

in which ΔH° (J mol⁻¹) and ΔS° (J K⁻¹ mol⁻¹) refers to the changes in enthalpy and entropy, while R and T are the gas constant (8.314 JK⁻¹ mol⁻¹) and temperature (K), respectively. The linear plot of ln $\frac{q_e}{C_e}$ against $\frac{1}{T}$ assisted the determination of ΔH° (kJ mol⁻¹) and ΔS° (kJ K⁻¹ mol⁻¹) as the slope and intercept, respectively.

Column adsorption experiments. The fixed bed adsorption behavior was examined in a glass column of diameter (3 cm), height (30 cm) and volume (250 mL) to investigate the treatment capacity of MWCNTs-KIAGNPs in a large scale. Particularly, the adsorption column was filled with 0.8 g of MWCNTs-KIAGNPs (average size (8.73 nm), bed height (2, 4 and 6 cm)), while both ends of the glass column were covered with gauze and cotton wool to enhance wastewater homogenous dispersion. The wastewater containing metal ions at the following initial concentrations (Cd(II) (11, 22 and 44 mg/L), Fe(II) (14, 28 and 56 mg/L), Cr(VI) (21.25, 42.5 and 85 mg/L) and Ni(II) (16.5, 33 and 66 mg/L)) were pumped into the dynamic glass column using a peristaltic pump from bottom to top at various flow rates (5, 7.5 and 10 mL/min). Subsequently, the effluent from the column was collected with vials at various time intervals and the metal ions concentration determined by AAS technique. Notably, the plot of breakthrough curves was based on normalized concentration at a specified time to initial concentration (C_t/C_o) against time profile⁴⁶. Accordingly, the breakthrough time (t_b) and exhaustion time (t_e) were evaluated at the C_t/C_o value equivalence of 5 and 95%, respectively^{42,47}. Above all, the capacity of wastewater treatment (V_b , mL; V_{total} , mL and m_{total} , mg) was calculated using Eqs. (10), (11) and (12)⁴².

$$V_b = Qt_b \quad (10)$$

$$V_{total} = Qt_{total} \quad (11)$$

$$m_{total} = \frac{C_o Qt_{total}}{1000} \quad (12)$$

The total amount of metal ions adsorbed (q_{total} , mg) was determined by the area under the $(C_o - C_t) \sim t$ curve indicated in Eq. (13), while the maximum adsorption capacity of MWCNTs-KIAGNPs (q_e , mg/g) was evaluated with the formula expressed in Eq. (14)⁴⁷.

$$q_{total} = \frac{Q}{1000} \int_{t=0}^{t=t_{total}} (C_o - C_t) dt \quad (13)$$

$$q_e = \frac{q_{total}}{m} \quad (14)$$

Meanwhile, the total metal ions adsorption (R_{total} , %) and the contact time of empty column (CTEC, min) were determined using Eqs. (15) and (16), respectively⁴².

$$R_{total} (\%) = \frac{q_{total}}{m_{total}} \times 100 \quad (15)$$

$$CTEC = \frac{\text{bedvolume}}{Q} \quad (16)$$

in which Q is the flow rate (mL/min), while t_b (min) and t_{total} (min) represents the time at breakthrough and saturation point, respectively. Also, V_b and V_{total} are the volume of wastewater treated at breakthrough and the total wastewater treated.

To further predict the dynamic behavior of Cd(II), Cr(VI), Fe(II) and Ni(II) ions adsorption by MWCNTs-KIAGNPs, the experimental data were fitted by Adams-Bohart (Eq. (17)) and Thomas (Eq. (18)) models to typically describe the breakthrough curves^{48,49}.

$$\frac{C_t}{C_o} = e^{K_{AB} C_o t - K_{AB} N_0 Z} \quad (17)$$

$$\frac{C_t}{C_o} = \frac{1}{1 + e^{\frac{K_T q_0 m}{Q} - K_T C_o t}} \quad (18)$$

where K_{AB} (L/(min mg)) and K_T (L/(min mg)) represents Adams-Bohart and Thomas kinetic constant, while N_0 (mg/L), F (cm/min) and Z (cm) refers to the concentration at saturation, linear velocity and depth of the column, respectively.

Batch/column regeneration tests. In order to evaluate the regeneration capacity of MWCNTs-KIAGNPs after the metal ions adsorption in a batch and continuous approach, the used nano adsorbent (20 mg) was treated using 0.5 M H_2SO_4 (50 mL) in a 250 mL conical flask. The solution was continuously stirred (150 rpm) at 40 °C for 2 h. Thereafter, Whatman grade 1 filter paper was utilized to filter the mixture, followed by washing with deionized water to achieve pH 7. The regenerated nano adsorbent was dried to constant weight prior to subsequent usage. Herein, the nano adsorbent performance studies were repeated 5 cycles and the effectiveness (η) determined using Eq. (19)⁵⁰.

$$\eta = \frac{C_o - C_e}{C_o} \times 100\% \quad (19)$$

Phytochemical	Qualitative	Quantitative (mg/g)
Alkaloids	+	31.66 ± 0.03
Phenols	+	102.23 ± 0.07
Tannins	+	5.14 ± 0.01
Flavonoids	+	20.94 ± 0.05
Saponins	+	25.15 ± 0.02
Terpenoids	+	3.84 ± 0.04
Steroids	–	ND
Glucosides	+	ND

Table 1. Phytochemical analysis of *Khaya ivorensis* (KI) leaf extract. Key: + = present; – = absent. ND not determined.

(a)				
Coded values	Temperature (°C)	pH	Volume of KI extract to Ag ⁺ solution (mL)	
– Level	40	8	2:8	
+ Level	70	10	8:2	
(b) Run				
	Temperature (°C)	pH	Volume of KI extract to Ag ⁺ solution (mL)	
1	40	8	2:8	
2	70	8	2:8	
3	40	10	2:8	
4	70	10	2:8	
5	40	8	8:2	
6	70	8	8:2	
7	40	10	8:2	
8	70	10	8:2	
(c)				
Run	Temperature (°C)	pH	Volume of KI extract to Ag ⁺ solution (mL)	Wavelength (nm)
1	70	8	8:2	448
2	70	8	2:8	449
3	70	10	2:8	450
4	40	8	8:2	447
5	40	10	8:2	447
6	40	10	2:8	449
7	40	8	2:8	448
8	70	10	8:2	447

Table 2. (a) 2³ factorial design matrix; (b) detailed experimental run for green synthesis of KIAgNPs and (c) wavelength response of green synthesized KIAgNPs.

in which C_o (mg/L) and C_e (mg/L) are the initial and equilibrium concentration of the metal ions, respectively.

Results and discussion

Qualitative and quantitative phytochemical determination. For further evaluation of the qualitative and quantitative presence of phytochemicals in KI leaf extract, phytochemical screening was carried out and the result presented in Table 1.

As shown in Table 1, the results revealed the presence of alkaloids, phenols, tannins, flavonoids, saponins, glucosides and terpenoids, while steroids and anthraquinones were absent. Moreso, the quantitative presence of the following phytochemicals; alkaloids (31.66 mg/g), phenols (102.23 mg/g), tannins (5.14 mg/g), flavonoids (20.94 mg/g), saponins (25.15 mg/g) and terpenoids (3.84 mg/g) were also identified. The result of the phytochemical screening revealed high concentration of biomolecules responsible for effective Ag⁺ bio-reduction to Ag⁰ and enhance the stabilization of KIAgNPs^{31,51}.

Optimization of green synthesis of KIAgNPs. A 2³ factorial design of experiment was used to investigate the effect of synthesis parameters such as temperature, pH and volume of AgNO₃ to KI extract, while the result is shown in Table 2c. According to Table 2c, optimum formation of KIAgNPs at the wavelength of

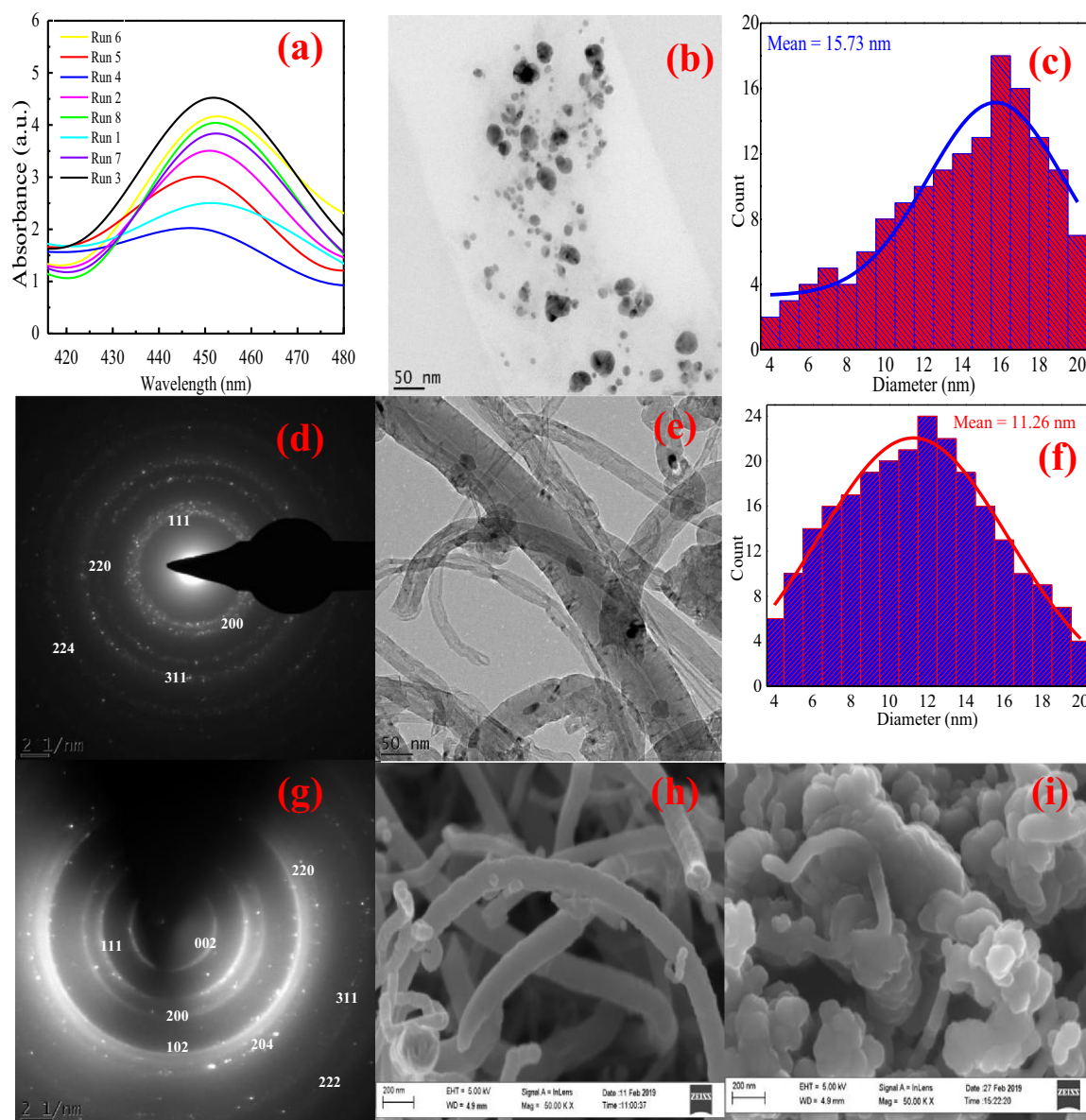


Figure 1. (a) UV-Vis spectra of 2^3 factorial design optimization of KAgNPs; HRTEM image of (b) KAgNPs; (c) diameter distribution of KAgNPs; (d) SAED pattern of KAgNPs; HRTEM image of (e) MWCNTs-KAgNPs; (f) Diameter distribution of MWCNTs-KAgNPs; (g) SAED pattern of MWCNTs-KAgNPs; HRSEM of MWCNTs-KAgNPs (h) before adsorption and (i) after adsorption.

450 nm was obtained at the temperature (70 °C), pH (10) and volume of AgNO_3 to KI extract (2:8), respectively. Although the formation of KAgNPs was observed visually through color change from yellow to brown, but UV-Vis spectroscopy excellently confirmed bio-reduction reaction of KAgNPs due to the surface plasmon resonance (SPR) band excitation in the UV-Vis region. The UV-Visible spectra of the biosynthesis of KAgNPs using 2^3 factorial design is displayed in Fig. 1a.

The result presented in Fig. 1a revealed that the absorbance peak occurred between 447 to 450 nm at the various process conditions, indicating the formation of KAgNPs. In all, the optimization of biosynthesis parameters showed that temperature increase lead to increment in SPR band and decrease in KAgNPs mean diameter³⁷. In addition, pH increase to 10 resulted to high absorption peak, indicating that -OH groups influences the bioreduction of Ag^+ to Ag^0 in a basic medium⁵¹. The capping, reduction and stabilization effects of KI leaves extract further demonstrated the use of Ag^+ solution in excess to ensure well dispersed and agglomerated free KAgNPs.

Typically, temperature (70 °C), pH (10) and volume of KI leaf extract to Ag^+ solution (2:8) showed the most intense peak at 450 nm. Statistical significance of KAgNPs synthesis parameters was analyzed using of variance (ANOVA). As shown in Table S1, pH exerted the highest influence on biosynthesis of KAgNPs with F-value of 16.77, followed by volume of KI extract to AgNO_3 solution and temperature with F-values of 12.42 and 4.36, respectively. The results on the biosynthesis of KAgNPs obtained in this study corroborated the findings reported previously by Tripathi et al.⁵² and Hamed et al.⁵³ using *Withania coagulans* and *Diospyros lotus* leaf extract,

respectively. Over the literature, it was previously reported that the peak of absorbance for AgNPs occur within the range of 400 to 450 nm^{37,53}. Hence, the results of this study confirm the bio synthesis of KIAgNPs of various particle sizes and shapes which could be ascribed to the differences in the observed SPR peaks⁵³.

Characterization of KIAgNPs and MWCNTs-KIAgNPs. HRTEM technique examined the micro-structure, morphology, size and crystalline nature of KIAgNPs and MWCNTs-KIAgNPs and the results are shown in Fig. 1b,e. From Fig. 1b, the HRTEM image of KIAgNPs exhibited a typical spherical and an ellipsoidal morphology demonstrating loosely bound particles. In addition, Fig. 1e revealed the deposited KIAgNPs on the surface of tubular network of MWCNTs. The HRTEM analysis of KIAgNPs and MWCNTs-KIAgNPs were measured in 50 nm range and the particle size distribution by histogram curves presented in Fig. 1c,f. An average particle size of 15.73 and 11.26 nm was obtained for KIAgNPs and MWCNTs-KIAgNPs which showed consistency with the evaluated particle size of XRD pattern using Debye Scherrer equation.

In Fig. 1d,g, the selected area of electron diffraction pattern (SAED) revealed bright ring patterns presence indicating the crystalline nature of the KIAgNPs and MWCNTs-KIAgNPs due to the different planes. Correspondingly, these patterns revealed fringes with bright round rings associated with (002), (111), (102), (200), (220), (204), (311) and (222) of Bragg's planes which also validate the crystallinity of the KIAgNPs and MWCNTs-KIAgNPs⁵⁴. The SAED pattern results showed good agreement with the XRD analysis, thereby suggesting the crystalline nature of the KIAgNPs and MWCNTs-KIAgNPs. The elemental chemical distribution of MWCNTs-KIAgNPs determined by energy dispersive X-ray spectrometer (EDS) is presented in Fig. S1. As observed from the result, strong signal of graphitic carbon and elemental silver nanoparticles were observed, which confirmed the successful incorporation of KIAgNPs onto the surface of MWCNTs. The presence of other components could be attributed to the KI leaf extract and analysis assays as reported over the literature^{37,54}.

The surface morphology of the MWCNTs-KIAgNPs were observed before and after adsorption using HRSEM as shown in Fig. 1h,i. Accordingly, the HRSEM image in Fig. 1h revealed the successful incorporation of a well distributed asymmetrical and spherical KIAgNPs on the surface of MWCNTs forming a tubular, intertwined network of MWCNTs-KIAgNPs structure. The cylindrical nanostructure of natural alignment transformed into ropes bound together by Van der Waals forces. Moreover, aggregated KIAgNPs were formed on the surface of the MWCNTs evident from the observed bright contrast on the surface of MWCNTs. Accordingly, the EDS elemental compositions presented in Table S2 revealed successful decoration of MWCNTs using KIAgNPs, which corresponds to the result of HRTEM analysis (Fig. S1). Typically in Fig. 1i, the morphology of MWCNTs-KIAgNPs slightly changed after adsorption process. An apparent aggregation of the chain-like morphology was observed with a slight reduction in the entangled tubular network of MWCNTs. The observed changes could be ascribed to the attachment of the adsorbed metal ions onto the surface of the MWCNTs-KIAgNPs as depicted by the EDS (Table S3). Similar observation was reported by Moazzen et al.³⁸ in the adsorption of phthalic acid esters (PAEs) from carbonated soft drinks using MWCNT-Fe₃O₄/Ag.

Furthermore, the XRD patterns of the synthesized KIAgNPs and MWCNTs-KIAgNPs are shown in Fig. 2a. The occurrence of characteristic crystalline peaks of AgNPs were observed at 2θ values of 38.32°, 44.50°, 64.59°, 77.55° and 81.81°. These observed diffraction peaks correspond to the following lattice planes (111), (200), (220), (311) and (222) of a typical face-centered cubic (FCC) structure of metallic silver crystal. The crystalline peaks of KIAgNPs in this study revealed significant agreement with other XRD patterns in the literature^{37,55}. It can also be seen from the XRD pattern of MWCNTs-KIAgNPs in Fig. 2a that diffraction peaks were observed at the 2 theta values; 26.55°, 38.32°, 44.50°, 50.97°, 64.59°, 74.65°, 77.55° and 81.81°. According to our previous study, the diffraction peaks for MWCNTs occurred at the 2 theta values of 26.55°, 50.97° and 74.65° typical for graphite carbon which were ascribed to the crystal planes (002), (102) and (204)³³. It is apparent from the XRD pattern of MWCNTs-KIAgNPs that the diffraction peaks at 38.32°, 44.50°, 64.59°, 77.55° and 81.81° indicate that KIAgNPs were strongly deposited on the surface of the MWCNTs^{27,38}. The crystal sizes of the KIAgNPs and MWCNTs-KIAgNPs was determined using Debye–Scherrer equation stated in Eq. (20)⁵⁴.

$$D = \frac{K\lambda}{\beta \cos\theta} \quad (20)$$

in which D (nm) represent the crystal size, while K denotes the shape factor (0.94). The parameters, λ (nm) and β (radians) are the X-ray wavelength (0.154 nm) and full width at half maximum (FWHM). Also, θ (degree) denotes the Bragg's angle. On the average, the crystallite sizes of the KIAgNPs and MWCNTs-KIAgNPs were 15.74 and 11.30 nm respectively and showed similarity to the result of HRTEM analysis in Fig. 1b.

Additionally, the evaluation of the surface properties of MWCNTs-KIAgNPs using BET technique demonstrated the values of 1236 ± 5.40 m²/g, 0.74 ± 0.02 cm³/g and 28 ± 0.50 nm for the surface area, pore volume and pore diameter. Importantly, the BET surface area of the MWCNTs-KIAgNPs was less than the surface area of 1250 m²/g reported for MWCNTs in our previous studies³³. The observed reduction in the surface properties of the nano adsorbent could be due to the dense occupation of the tubular linkages of the MWCNTs by decoration with KIAgNPs. In the light of the observed decrease in surface area of MWCNTs-KIAgNPs after decoration with KIAgNPs, it was also reported that surface area of GnzVI/PAC and MWCNTs@SiO₂-NH₂ reduced after the incorporation of GnzVI and SiO₂-NH₂^{56,57}.

The FTIR spectrum of the MWCNTs-KIAgNPs before and after adsorption of Cd(II), Cr(VI), Fe(II) and Ni(II) ions is shown in Fig. 2b. As can be seen in Fig. 2b, characteristic peaks were assigned to the following absorption bands: 895 (C–H), 1250 (C=O), 1959 (C≡C), 2114 (C≡C), 2365 (C≡C) and 2835 (C–H) cm⁻¹, respectively³⁸. The observed peaks were attributed to the bending and stretching due to alkene, alkane, alkyne and phenolic groups. Also, the observed absorption bands on MWCNTs-KIAgNPs before and after adsorption at 1078 and 3000 cm⁻¹ were attributable to the vibrational stretching of C–O and O–H due to alkanes and carboxylic groups³⁸.

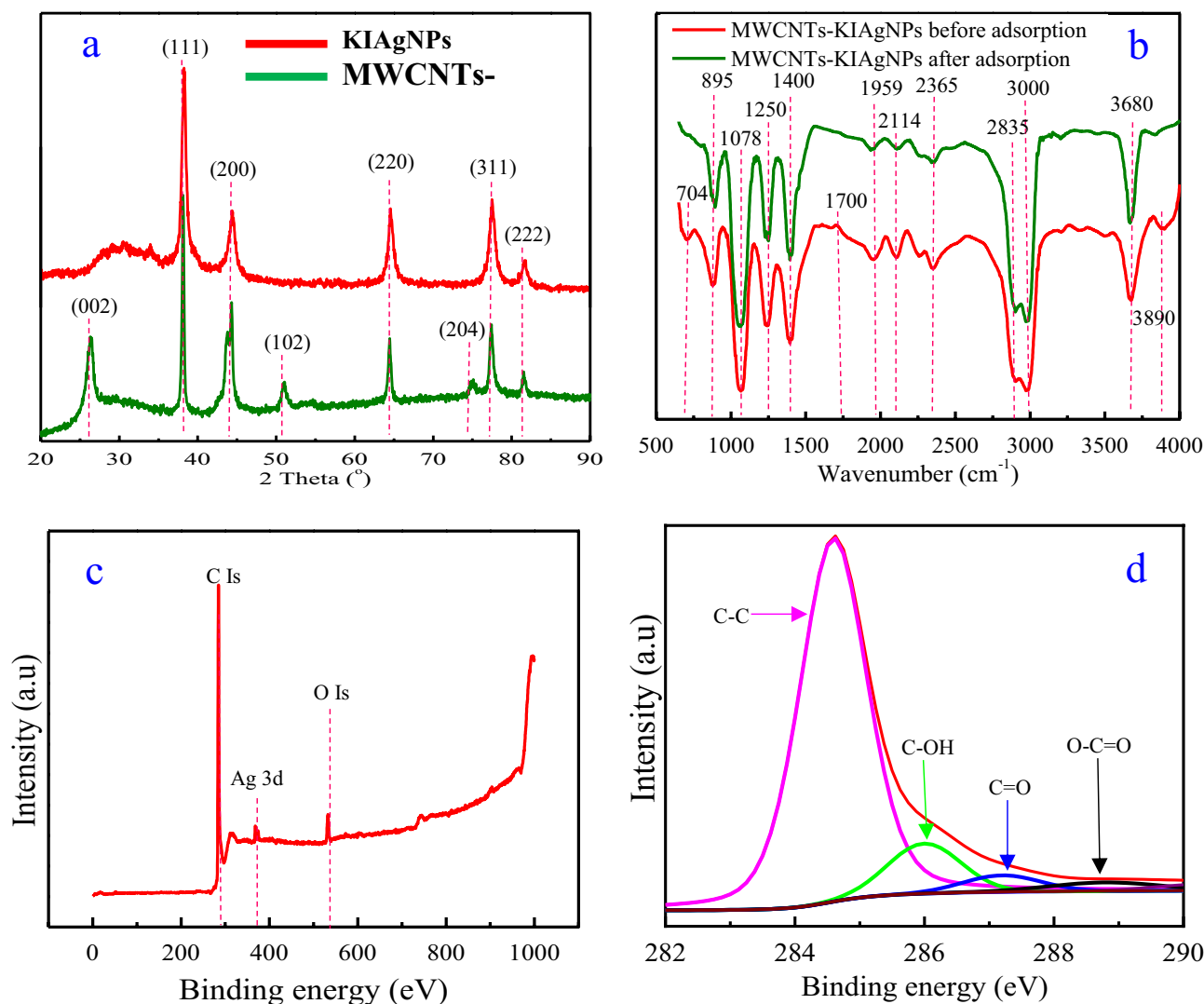


Figure 2. XRD of (a) KI AgNPs and MWCNTs-KI AgNPs; (b) FTIR of MWCNTs-KI AgNPs before and after adsorption; (c) XPS full survey scan spectra of MWCNTs-KI AgNPs; (d) high resolution C 1s spectra of MWCNTs-KI AgNPs.

Noticeably, a very strong peak peculiar to KI AgNPs was found at 1700 cm^{-1} which corresponds to C=O stretching vibration of the amine³⁷. Also, the peak at 1400 cm^{-1} could be attributed to C=C stretching and N-H vibrations phenolic and amine groups contained in the KI extract³⁸. Notably, the peak at 3680 cm^{-1} on MWCNTs-KI AgNPs before and after adsorption were assigned to the O-H stretching frequencies of the hydroxyl group³⁸. Remarkably, Fig. 2b revealed two distinctive peaks on MWCNTs-KI AgNPs prior to adsorption at 3890 cm^{-1} which corresponds to the stretching modes overlap of correlative amines, free amines and hydroxyl groups (NH_2 , $-\text{NH}-$ and $-\text{OH}$)⁴². Also, the peak at 704 cm^{-1} could be attributed to C-H bend due to alkene. However, the disappearance of absorption bands at 704 and 3890 cm^{-1} on the MWCNTs-KI AgNPs after adsorption could be attributed to the attached metal ions on the surface of the nano adsorbent.

In this study, FTIR analysis validated that Ag^+ reduction occurred due to various functional groups: flavonoids, tannins, phenols, terpenoids and polysaccharides present in the KI extract³⁷. Furthermore, carbonyl groups bind to metals better than amino acids and proteins which principally forms coating layer on the metal nanoparticles surface, thereby suitably inhibiting accumulation and improving KI AgNPs stability⁵⁸. More still, amine ($-\text{NH}$), carboxyl ($-\text{C}=\text{O}$) and hydroxyl ($-\text{OH}$) groups constituents of KI extract enhances the stability of KI AgNPs³².

To further examine the elemental and surface oxidation states of the nano adsorbent composite, XPS analysis was conducted and the result shown in Fig. 2c,d. Notably, Fig. 2c of MWCNTs-KI AgNPs clearly illustrated the appearance of three pronounced peaks at 284 , 374 and 530 eV , indicating the nano adsorbent was predominantly composed of elemental C, Ag and O²⁷. Likewise, the deconvolution of C (1s) spectrum presented in Fig. 2d revealed four peaks at 284 , 286 , 287.5 and 288.7 eV corresponding to C-C, C-OH, C=O and O-C=O bonds²⁶. The XPS analysis showed good agreement with the FTIR (Fig. 2b) result, thereby confirming the presence of

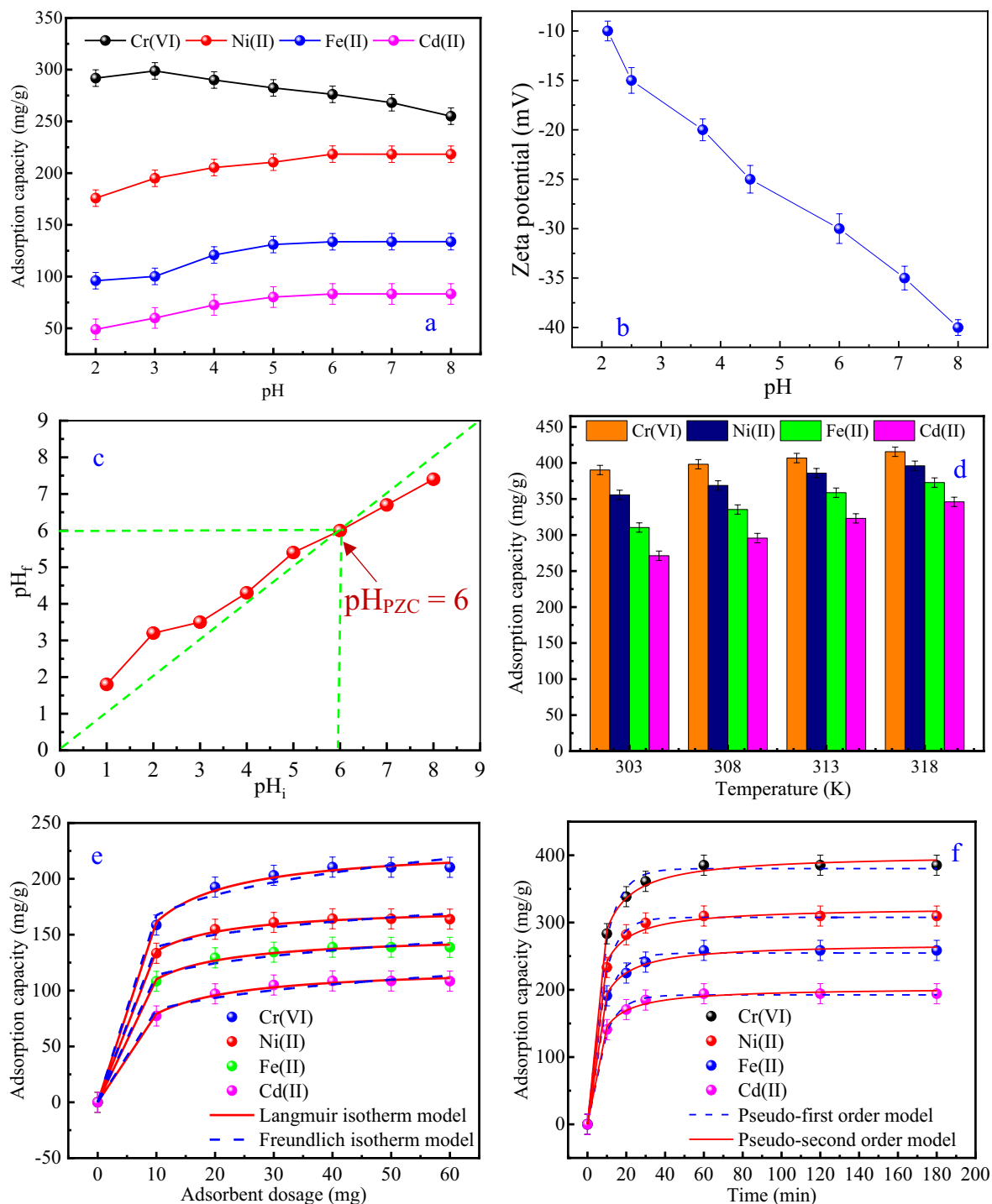


Figure 3. (a) Effect of pH on the adsorption of metal ions by MWCNTs-KIAGNPs; (b) point of zero charge pH (pH_{PZC}) of MWCNTs-KIAGNPs; (c) zeta potentials of MWCNTs-KIAGNPs; (d) influence of temperature on the uptake of Cr(VI), Ni(II), Fe(II) and Cd(II) ions by MWCNTs-KIAGNPs; (e) Langmuir and Freundlich isotherm model curves of MWCNTs-KIAGNPs adsorption towards Cr(VI), Ni(II), Fe(II) and Cd(II); (f) pseudo-first order and pseudo-second order kinetic model for Cr(VI), Ni(II), Fe(II) and Cd(II) adsorption by MWCNTs-KIAGNPs.

the reported functional groups and validating the observed presence of the incorporated materials onto the fabricated MWCNTs-KIAGNPs.

Batch adsorption performance. *Effect of solution pH.* Due to the interactions of the metal ions and adsorbents surface property in aqueous conditions³⁹, it is important to examine the influence of solution pH on the adsorption of Cr(VI), Ni(II), Fe(II) and Cd(II) on MWCNTs-KIAGNPs. As presented in Fig. 3a, it is clearly

Adsorbate	$q_{e, \text{exp}}$ (mg/g)	Langmuir isotherm model parameters					Freundlich isotherm model parameters			
		q_m (mg/g)	K_L (L min ⁻¹)	R_L	R^2	X^2	K_F (mg/g)	n_F	R^2	X^2
Cr(VI)	210.513 ± 0.001	229.540 ± 0.001	0.237 ± 0.002	0.047 ± 0.003	0.971	11.946	119.203 ± 0.002	6.777 ± 0.001	0.844	64.355
Ni(II)	164.256 ± 0.002	174.784 ± 0.006	0.342 ± 0.003	0.042 ± 0.001	0.962	5.563	108.404 ± 0.001	9.240 ± 0.002	0.814	27.169
Fe(II)	138.775 ± 0.003	149.552 ± 0.005	0.279 ± 0.001	0.060 ± 0.002	0.967	4.621	84.465 ± 0.003	7.747 ± 0.001	0.833	23.662
Cd(II)	108.650 ± 0.002	121.026 ± 0.003	0.189 ± 0.004	0.108 ± 0.001	0.965	5.330	55.186 ± 0.001	5.691 ± 0.002	0.838	24.838

Table 3. Calculated isotherm model parameters for metal ions adsorption by MWCNTs-KIAGNPs.

evident that the adsorption effectiveness of MWCNTs-KIAGNPs towards Ni(II), Fe(II) and Cd(II) ions increased with increasing pH from 2 to 6, while Cr(VI) increased from 2 to 3. The adsorbed amount of Cr(VI) on the adsorbent further reduced with increase in pH above 3.

As can be seen from the figure, further increment in the removal of Cd(II), Ni(II) and Fe(II) were not noticeable beyond pH 6. Overall, the maximum adsorption capacity of Cd(II), Fe(II) and Ni(II) were obtained as 83.20, 133.63 and 218.32 mg/g, respectively at the pH of 6. On the other hand, the maximum adsorption capacity of Cr(VI) was obtained as 298.12 mg/g at the pH of 3. As reported previously, HCrO_4^- , CrO_4^{2-} , $\text{Cr}_2\text{O}_7^{2-}$, $\text{Cr}_3\text{O}_{10}^{3-}$ and $\text{Cr}_4\text{O}_{13}^{4-}$ are the various forms of chromium⁶⁰ in a solution. Meanwhile, HCrO_4^- and $\text{Cr}_2\text{O}_7^{2-}$ are the dominant form of Cr(VI) in the solution at low pH, while CrO_4^{2-} are present at higher pH⁶¹. The higher removal of Cr(VI) at low pH (3) may be attributed to increase in ionizing ability of Cr(VI), formation of HCrO_4^- and positive surface formation⁶². Therefore, enhanced electrostatic attraction between the positively charged surface of MWCNTs-KIAGNPs in acidic medium and HCrO_4^- species was generated, which favored higher Cr(VI) adsorption. However, at higher pH the HCrO_4^- transformed to CrO_4^{2-} which resulted to reduce amount of Cr(VI) due to force of repulsion between the CrO_4^{2-} and negatively charged adsorbent surface. The decrease in Cd(II), Fe(II) and Ni(II) adsorption at low pH values may be due to the fierce adsorption competition between the highly positive H^+ and the metal ions (Cd(II), Fe(II) and Ni(II)) for the occupation of the functional adsorption sites. Most importantly, the reduction in negative surface charge of MWCNTs-KIAGNPs may be due to protonation which enhanced the adsorbents positively charged surface, thereby correspond to decrease in electrostatic attraction towards Ni(II), Fe(II) and Cd(II) adsorption. However, the deprotonation phenomenon of MWCNTs-KIAGNPs surface at high pH resulted in increased negative charge of the adsorbent which enhanced the electrostatic interaction leading to maximum adsorption capacity. Correspondingly, the electrophoretic performance and surface charge of the MWCNTs-KIAGNPs were obtained by the zeta potential as shown in Fig. 3b. Importantly too, Fig. 3c revealed that the pH point of zero charge (pH_{PZC}) of MWCNTs-KIAGNPs was obtained as 6. This indicates that the surface of MWCNTs-KIAGNPs was positively charged at $\text{pH}_{\text{PZC}} < 6$, while the adsorbent surface was negatively charged at $\text{pH}_{\text{PZC}} > 6$ ¹⁵. In all, pH 6 was selected for further investigation of Cd(II), Ni(II) and Fe(II) adsorption, while pH 3 was utilized for Cr(VI) adsorption due to its optimal adsorption values for all the metal ions without precipitation to metal hydroxides⁵⁹. Similar pH impact on the adsorption of Cr(VI), Ni(II), Fe(II) and Cd(II) ions have been previously reported over the literature^{61,63,64}.

Effect of temperature. The influence of temperature on Cr(VI), Ni(II), Fe(II) and Cd(II) ions adsorption by MWCNTs-KIAGNPs was examined at 303 to 318 K. As shown in Fig. 3d, the adsorption capacities were observed to increase with increasing temperatures and optimum adsorption capacities of Cr(VI) (416 mg/g), Ni(II) (396 mg/g), Fe(II) (372 mg/g) and Cd(II) (346 mg/g) were achieved at the temperature of 318 K. The favorability of the metal ions capture by MWCNTs-KIAGNPs may be linked to the endothermic reaction characteristics which reduced solution viscosity, increased external mass transfer and metal ions diffusion to the pores of the MWCNTs-KIAGNPs. Overall, metal ions adsorption were thermally governed due to activation energy generation by temperature thereby leading to aggregation ascribed to increase in kinetic energy and metal ions collision with the binding sites of the nano adsorbent⁴⁹.

Adsorption isotherm. The influence of MWCNTs-KIAGNPs dosage towards the effective adsorption of metal ions was investigated in the range of 10 to 60 mg/L in order to examine the contact areas between the adsorbent and metal ions. According to Fig. 3e, increase in metal ions adsorption capacity was noticed with increasing adsorbent dosage of 10 to 40 mg/L. Notably, the observed proportional increase in adsorption capacity with adsorbent dosage increase could be attributed to increased surface area of the MWCNTs-KIAGNPs and the abundant availability of adsorption sites. However, further increase in adsorbent dosage beyond 40 mg/L showed insignificant change in adsorption capacity which may be due to the saturation and over saturation of the adsorption sites⁶⁵. Therefore, 40 mg/L was identified as the optimum amount of adsorbent for metal ions removal in this study. Importantly, higher adsorption capacity of 210.51, 164.26, 138.78 and 108.65 mg/g, respectively were obtained for Cr(VI), Ni(II), Fe(II) and Cd(II) adsorption by MWCNTs-KIAGNPs.

Subsequently, Langmuir and Freundlich isotherm model were used to fit the correlative data to assess the characteristic interface and MWCNTs-KIAGNPs affinity towards Cr(VI), Ni(II), Fe(II) and Cd(II) adsorption as revealed in Fig. 3e. Accordingly, a rapid-slow trend in adsorption was evident signaling that the availability of large adsorption sites could enhance adsorption capacity, while slower adsorption was attributed to the presence of limited adsorption sites⁶⁶.

The isotherm parameters from the Langmuir and Freundlich models were calculated and the various values presented in Table 3. The removal of the metal ions was better fitted to Langmuir model due to the higher

Adsorbate	C_0 (mg L ⁻¹)	$q_{e, exp}$ (mg g ⁻¹)	Pseudo-first order kinetic model parameters				Pseudo-second order kinetic model parameters			
			k_1 (min ⁻¹)	$q_{e, cal}$ (mg g ⁻¹)	R^2	X^2	k_2 (g·mg ⁻¹ ·min ⁻¹) × 10 ⁻⁴	$q_{e, cal}$ (mg g ⁻¹)	R^2	X^2
Cr(VI)	85.00	385.220 ± 0.004	0.128 ± 0.002	401.24 ± 0.003	0.935	106.411	1.723 ± 0.001	380.384 ± 0.005	0.968	53.030
Ni(II)	66.00	309.696 ± 0.006	0.137 ± 0.005	322.689 ± 0.002	0.926	67.091	1.557 ± 0.003	307.780 ± 0.004	0.980	18.501
Fe(II)	56.00	258.580 ± 0.003	0.128 ± 0.001	268.69 ± 0.004	0.910	65.874	0.976 ± 0.004	264.989 ± 0.003	0.973	19.594
Cd(II)	44.00	194.150 ± 0.012	0.124 ± 0.003	203.419 ± 0.005	0.949	22.773	0.767 ± 0.002	192.137 ± 0.002	0.963	16.836

Table 4. Calculated kinetic model parameters for metal ions adsorption by MWCNTs-KIAGNPs.

Adsorbate	Temperature (K)	ΔG° (kJ/mol)	ΔH° (kJ/mol)	ΔS° (J/mol)
Cr(VI)	303	-1155.28 ± 0.1	2153.33 ± 10.00	124.34 ± 4.00
	308	-1777.00 ± 0.003		
	313	-2920.44 ± 0.06		
	318	-4163.88 ± 0.02		
Ni(II)	303	-934.14 ± 0.04	1956.03 ± 9.20	118.61 ± 3.00
	308	-1592.18 ± 0.02		
	313	-2808.25 ± 0.06		
	318	-4024.32 ± 0.05		
Fe(II)	303	-875.14 ± 0.03	1787.34 ± 7.50	111.50 ± 2.00
	308	-1367.64 ± 0.01		
	313	-2552.63 ± 0.07		
	318	-3637.63 ± 0.04		
Cd(II)	303	-852.14 ± 0.02	1706.70 ± 6.10	102.35 ± 1.00
	308	-1363.91 ± 0.04		
	313	-2387.45 ± 0.03		
	318	-3410.98 ± 0.01		

Table 5. Thermodynamic parameters for Cr(VI), Ni(II), Fe(II) and Cd(II) adsorption by MWCNTs-KIAGNPs.

correlation coefficient closer to 1 ($R^2 = 0.971, 0.962, 0.967$ and 0.965 for Cr(VI), Ni(II), Fe(II) and Cd(II) adsorption) and lower X^2 values (11.946, 5.563, 4.621 and 5.330 for Cr(VI), Ni(II), Fe(II) and Cd(II)). Accordingly, a homogenous monolayer coverage of the Cr(VI), Ni(II), Fe(II) and Cd(II) ions on the surface of MWCNTs-KIAGNPs were dominant in the chemisorption controlled adsorption process, while the higher correlation coefficient validated the electrostatic interaction mechanism⁴².

Of particular attention is that the adsorption intensity (n_F) of all the metal ions were greater than 1, indicating possible favorability of metal ions uptake. Furthermore, the calculated maximum adsorption capacities were obtained as 229.540, 174.784, 149.552 and 121.026 mg/g for Cr(VI), Ni(II), Fe(II) and Cd(II) ions, respectively. Additionally, the preferential adsorption and the enhanced adsorption capacity of some of the metal ions over others could be linked to the differences in their ionic radius. For instance, the ionic radius of the metal ions are Cr(VI) (0.44 Å), Ni(II) (0.56 Å), Fe(II) (0.64 Å) and Cd(II) (0.78 Å)⁶⁷⁻⁶⁹. It is apparent that metals with smaller ionic radius diffuse faster onto the binding sites of the adsorbent, compared with metals with higher ionic radius⁶⁷. Based on the ionic radius, the superior adsorption of the metal ions onto MWCNTs-KIAGNPs were in the range Cr(VI) > Ni(II) > Fe(II) > Cd(II).

Adsorption kinetics. Further investigation of time-dependent curves of Cd(II), Cr(VI), Ni(II) and Fe(II) ions adsorption by MWCNTs-KIAGNPs were carried out in the range of 10–180 min as shown in Fig. 3f. Obviously, a rapid increase in the adsorption capacities of the metal ions were observed in the first 60 min which was ascribed to the increased diffusion of the metal ions to the rich adsorption sites and the presence of strong attractive forces between the metal ions and MWCNTs-KIAGNPs⁷⁰. Subsequently, the adsorption capacity decreased gradually with further increase in time beyond 60 min due to the depletion of the binding sites⁶⁵.

Herein, the experimental data were fitted by pseudo-first order and pseudo-second order kinetics as shown in Fig. 3f, while the parameters obtained from the kinetic equations are presented in Table 4. Based on the higher correlation coefficient (R^2) and lower error (X^2) values, pseudo-second order kinetic equation suitably fit the adsorption data for Cr(VI), Ni(II), Fe(II) and Cd(II) ions. Notably, the adsorption of Cr(VI), Ni(II), Fe(II) and Cd(II) ions corresponding to pseudo-second order kinetics clearly affirms that the adsorption of the metal ions by MWCNTs-KIAGNPs were dominated majorly by chemisorption behavior⁶⁶.

Adsorption thermodynamics. To further evaluate the thermodynamic parameters of Cr(VI), Ni(II), Fe(II) and Cd(II) ions adsorption by MWCNTs-KIAGNPs, the thermodynamic plots and evaluated parameters are shown in Fig. S2 and Table 5, respectively.

Adsorbent	Adsorbate	pH	Temp. (K)	Time (min)	Surface area (m ² /g)	q _m (mg/g)	Isotherm/kinetics	References
α-Fe ₂ O ₃ @C	Cr(VI)	3	298	360	ND	76.92	Langmuir/PSO	Trang et al. ⁶⁰
GnZVI/PAC	Cr(VI)	2	323	80	107	53.48	Langmuir/PSO	Khosravi et al. ⁵⁷
DWHR	Cr(VI)	3	298	120	ND	1.28	Freundlich/PSO	Kumar and Chauhan ⁷³
CES	Ni(II)	6.5	298	960	ND	163.6	Langmuir/PSO	Peng et al. ⁷⁴
Goethite	Ni(II)	9	363	60	5.12	0.943	Langmuir/PSO	Dash et al. ⁶³
BTMC	Ni(II)	5	298	30	209	57.14	Langmuir/ND	Anitha et al. ⁷⁵
Ca-Pal	Fe(II)	6	298	10	297	3.71	Langmuir/ND	Lazaratou et al. ⁶⁴
Sepiolite	Fe(II)	5	293	30	200	12	Langmuir/ND	Kocaoba ⁷⁶
PSBAC	Fe(II)	3	303	90	1500	41.66	Temkin/PSO	Kaveeshwar et al. ⁷²
SLMO	Cd(II)	6	298	720	17.09	26.24	Langmuir/PSO	Zhang et al. ⁶²
Fe-BTC	Cd(II)	7	318	20	289.33 ± 1.60	9.55	Langmuir–Freundlich/ND	Zhang et al. ⁷⁰
CABs-MO	Cd(II)	6.5	298	720	2.04 ± 0.002	63.6	Langmuir/PSO	Shim et al. ⁷⁷
MWCNTs-KIAGNPs	Cr(VI)	3	313	60	1236 ± 5.40	229.540 ± 0.001	Langmuir/PSO	This study
MWCNTs-KIAGNPs	Ni(II)	6	313	60	1236 ± 5.40	174.784 ± 0.006	Langmuir/PSO	This study
MWCNTs-KIAGNPs	Fe(II)	6	313	60	1236 ± 5.40	149.552 ± 0.005	Langmuir/PSO	This study
MWCNTs-KIAGNPs	Cd(II)	6	313	60	1236 ± 5.40	121.026 ± 0.003	Langmuir/PSO	This study

Table 6. Comparison of adsorption parameters among the adsorbates and various adsorbents. *PFO* pseudo-first order, *PSO* pseudo-second order, *ND* not determined.

The results presented in Table 5 revealed negative values of ΔG° at different temperatures, indicating spontaneity of metal ions removal by MWCNTs-KIAGNPs. Correspondingly, the observed decrease of ΔG° values with temperature increase suggests enhanced adsorption at higher temperatures. Additionally, the metal ions adsorption was endothermic in nature due to the positive values of ΔH° indicating spontaneity increase and interaction with MWCNTs-KIAGNPs. Notably, the obtained values of ΔH° Cr(VI) (2153.33), Ni(II) (1956.03), Fe(II) (1787.34) and Cd(II) (1706.70) were higher than 40 kJ/mol, thereby confirmed that the adsorption process was chemisorption controlled⁷¹. Moreover, the ΔS° positive values Cr(VI) (124.34), Ni(II) (118.61), Fe(II) (111.50) and Cd(II) (102.35) revealed increasing randomness at Cr(VI)/Ni(II)/Fe(II)/Cd(II)-MWCNTs-KIAGNPs solution interface.

Comparison with other adsorbents. Additionally, the adsorption capacities of the metal ions obtained in this study have been compared with previous studies as shown in Table 6. Remarkably, Table 6 revealed that MWCNTs-KIAGNPs showed higher adsorption capacity compared to the adsorption capacities by the various adsorbents from the literature. The observed higher adsorption capacity in this study could be attributed to the high surface area and functional groups of MWCNTs-KIAGNPs that provided massive binding sites for the adsorption of the metal ions. Although a higher surface area of 1500 m²/g were reported for PSBAC, but the adsorption capacity of 41.66 mg/g for Fe(II) removal was relatively small compared to the result of this study⁷². The observed differences may be due to the variations in the functional groups and structural nature of the materials.

Column adsorption performance. Fixed bed adsorption in a continuous flow seemingly demonstrates strong favorability for enhanced practical application. In all, fixed bed model parameters determination may aid the industrial scale up of the adsorption process without further experimentation⁴⁷.

Therefore, investigation of the capture capacity of MWCNTs-KIAGNPs for Cr(VI), Ni(II), Fe(II) and Cd(II) ions in a continuous flow adsorption was performed. More than that, parameters influencing the dynamic adsorption behavior were examined by varying the initial metal concentration, bed height and flow rate on the breakthrough curve. Thereafter, the simulation of the experimental data using Thomas and Adams-Bohart model were accomplished.

Effect of bed height, inlet concentration and flow rate. The influence of bed height (2, 4 and 6 cm) towards Cr(VI), Ni(II), Fe(II) and Cd(II) ions removal in dynamic adsorption system was examined as shown in Fig. S3(a, d, g and j), while the determined parameters are presented in Table 7. As observed from the figures, decrease in bed height accelerated the duration for the breakthrough and saturation, culminating to the early bed saturation. On the other hand, increase in bed height enhanced both the time for breakthrough and exhaustion due to the longer length and contact time of the mass transfer zone (MTZ) at each column ends⁷⁸. Particularly, increasing the bed length resulted to increase in the quantity of MWCNTs-KIAGNPs, thereby providing more adsorption

Adsorbate	C (mg/L)	Q (mL/min)	Z (cm)	t_b (min)	q_{total} (mg/g)	q_e (mg)	L_{MTZ} (cm)	Thomas model			Adams-Bohart model		
								K_{TH}	q_0	R^2	K_{AB}	N_0	R^2
Cr(VI)	21.25	5.00	2	480	84.163	33.665	1.762	0.00030	35.923	0.966	0.00016	302.724	0.700
	21.25	5.00	4	1200	125.438	44.799	3.872	0.00029	46.368	0.991	0.00012	291.053	0.768
	21.25	5.00	6	1600	158.625	52.875	5.040	0.00027	53.668	0.999	0.00011	134.208	0.832
	42.50	5.00	4	720	108.525	38.759	4.352	0.00031	40.901	0.978	0.00017	259.935	0.743
	85.00	5.00	4	480	84.750	30.268	3.995	0.00035	31.346	0.973	0.00024	223.623	0.751
	21.25	7.50	4	720	98.694	35.248	3.619	0.00032	38.197	0.990	0.00015	210.398	0.789
	21.25	10.00	4	480	75.975	27.134	3.010	0.00034	28.629	0.980	0.00019	187.707	0.776
Ni(II)	16.50	5.00	2	720	78.225	31.290	1.810	0.00029	35.106	0.964	0.00011	199.466	0.680
	16.50	5.00	4	1200	112.397	40.142	3.524	0.00027	42.543	0.993	0.00010	236.755	0.772
	16.50	5.00	6	1600	143.192	47.731	5.040	0.00026	48.119	0.997	0.00009	275.309	0.793
	33.00	5.00	4	720	101.705	36.323	4.348	0.00034	37.096	0.997	0.00013	229.454	0.887
	66.00	5.00	4	480	72.626	25.938	3.706	0.00038	26.427	0.995	0.00015	208.611	0.748
	16.50	7.50	4	720	89.094	31.819	3.219	0.00030	34.341	0.992	0.00016	215.199	0.795
	16.50	10.00	4	240	68.630	24.511	2.914	0.00032	27.891	0.989	0.00019	172.134	0.773
Fe(II)	14.00	5.00	2	720	70.320	28.128	1.810	0.00022	26.179	0.981	0.00008	176.642	0.764
	14.00	5.00	4	1400	103.050	36.804	3.524	0.00021	35.597	0.992	0.00007	192.067	0.764
	14.00	5.00	6	1800	125.740	41.913	5.280	0.00020	41.792	0.999	0.00006	219.307	0.817
	28.00	5.00	4	960	94.980	33.921	3.876	0.00023	44.171	0.985	0.00009	191.292	0.723
	56.00	5.00	4	480	67.804	24.216	3.349	0.00026	25.900	0.976	0.00011	164.414	0.681
	14.00	7.50	4	720	86.948	31.053	3.519	0.00022	32.103	0.973	0.00008	176.618	0.719
	14.00	10.00	4	240	70.020	22.007	3.114	0.00024	23.417	0.973	0.00012	153.409	0.732
Cd(II)	11.00	5.00	2	720	64.320	25.728	1.810	0.00020	26.702	0.975	0.00005	105.026	0.777
	11.00	5.00	4	1400	92.625	33.080	3.658	0.00019	35.951	0.986	0.00006	167.225	0.801
	11.00	5.00	6	1800	114.055	38.018	5.280	0.00017	40.262	0.992	0.00007	200.772	0.831
	22.00	5.00	4	960	77.330	27.618	3.962	0.00022	27.919	0.988	0.00008	185.979	0.770
	44.00	5.00	4	480	59.260	21.164	3.231	0.00026	22.431	0.990	0.00010	155.660	0.749
	11.00	7.50	4	960	68.493	24.462	3.380	0.00021	25.451	0.983	0.00009	163.725	0.786
	11.00	10.00	4	720	54.520	19.471	2.810	0.00024	17.574	0.982	0.00012	148.019	0.663

Table 7. Determined parameters of breakthrough curves and continuous adsorption models for Cr(VI), Ni(II), Fe(II) and Cd(II) adsorption by MWCNTs-KIAGNPs.

sites for Cr(VI), Ni(II), Fe(II) and Cd(II) ions uptake. Notably, improved metal ions adsorption was attained by increasing the bed length and may be attributed to the availability of enormous time for the metal ions to interact with the MWCNTs-KIAGNPs.

The calculated parameters in Table 7 indicate that the maximum adsorption capacities (q_e) for Cr(VI), Ni(II), Fe(II) and Cd(II) ions adsorption using bed length of 6 cm were obtained as 52.875, 47.731, 41.913 and 38.018 mg/g, respectively. Importantly, the trend of bed length impact on dynamic adsorption in this study showed strong collaboration with the literature on the increment of total adsorbing surface area of MWCNTs-KIAGNPs using highest bed length due to abundant binding sites for adsorption^{78,79}. Comparatively, the obtained continuous adsorption capacities in this study were relatively lower than the values in batch process and may be ascribed to the limitations of mass transfer provided by fixed bed against complete mixing of a batch reactor. Likewise, the preferential adsorption in the order of Cr(VI) > Ni(II) > Fe(II) > Cd(II) may be due to the atomic radii of the metal ions.

The influent concentrations of Cr(VI), Ni(II), Fe(II) and Cd(II) ions were varied as demonstrated in Table 7. Accordingly, Fig. S3(b, e, h and k) illustrates the steepness of the breakthrough curves gradient with higher influent concentration of the metal ions. Of specific emphasis is the clear reduction in breakthrough time (t_b) with increasing influent concentration as shown in Table 7. As expected, the observed behavior may be credited to the overwhelming driving force provided by the higher inlet concentration difference in order for the adsorption process to overpower the resistance of mass transfer⁴⁷. Apparently, shorter exhaustion time was also evident as the influent concentration of the metal ions increased leading to faster saturation of the binding sites⁷⁸. In other words, increase in influent metal concentration obviously enhanced the removal rate of the metal ions due to the corresponding increase in the driving force for mass transfer⁷⁹. Remarkably, Table 7 reveals that the optimal column adsorption capacity (q_e) of Cr(VI) (44.799 mg/g), Ni(II) (40.142 mg/g), Fe(II) (36.804 mg/g) and Cd(II) (35.080 mg/g) were obtained at low influent concentrations of Cr(VI) (21.25 mg/L), Ni(II) (16.50 mg/L), Fe(II) (14.00 mg/L) and Cd(II) (11.00 mg/L). The findings of this study showed consistency with the previously reported literature on continuous flow adsorption system and notably revealed that fixed bed adsorption is inlet concentration dependent^{78,79}.

Parameters	Raw wastewater concentration	Concentration after treatment using MWCNTs-KIAGNPs		Permissible standards	
		Batch adsorption	Fixed bed adsorption	US, EPA ⁸²	WHO ⁸³
Chromium (mg/L)	85.00 ± 0.06	0.020 ± 0.006	0.030 ± 0.004	0.1	0.05
Nickel (mg/L)	66.00 ± 0.03	0.040 ± 0.005	0.020 ± 0.002	0.1	0.07
Iron (mg/L)	56.00 ± 0.02	0.200 ± 0.002	0.180 ± 0.003	0.50	0.3
Cadmium (mg/L)	44.00 ± 0.01	0.002 ± 0.001	0.001 ± 0.001	0.005	0.003
pH	3.90 ± 0.05	6.95 ± 0.75	6.80 ± 0.60	6.5–8.5	5.5–8.5
TDS (mg/L)	36,49 ± 30.50	455.00 ± 5.80	432.00 ± 7.50	500	600
BOD (mg/L)	123.00 ± 0.40	8.33 ± 0.50	9.43 ± 0.52	10	10
COD (mg/L)	24,615 ± 25.30	12.34 ± 0.10	16.00 ± 0.20	40	40
Nitrate (mg/L)	489.00 ± 0.25	23.81 ± 0.15	30.13 ± 1.10	40	50
Chloride (mg/L)	1,980.00 ± 8.20	65.00 ± 1.22	76.08 ± 1.50	200	250
Phosphate (mg/L)	190.40 ± 0.65	0.20 ± 0.04	0.10 ± 0.001	1	0.5
Fluoride (mg/L)	103.00 ± 5.40	1.30 ± 0.03	1.15 ± 0.02	2	1.5
Sulphate (mg/L)	2790.00 ± 2.70	81.03 ± 2.40	48.62 ± 1.20	200	250

Table 8. Physico-chemical parameters of chemical industry wastewater and treated water in batch and fixed bed column.

Further investigation on the influence of flow rate (5, 7.5 and 10 mL/min) on the breakthrough curve was examined for Cr(VI), Ni(II), Fe(II) and Cd(II) ions adsorption by MWCNTs-KIAGNPs as shown in Fig. S3(c, f, i and l). All in all, metal ions had ample time for interaction with MWCNTs-KIAGNPs at lower flow rates culminating to the observed higher removal capacity of Cr(VI), Ni(II), Fe(II) and Cd(II) ions⁴⁷. As demonstrated through the determined parameters in Table 7, increase in flow rate from 5 to 10 mL/min led to clear decrease in the adsorption capacity (q_e) of metal ions from 44.799 to 27.134 mg/g for Cr(VI), 40.142 to 24.511 mg/g for Ni(II), 36.804 to 22.007 mg/g for Fe(II) and 33.080 to 19.471 mg/g for Cd(II). Not only that, the maximum total adsorbed amount (q_{total}) of Cr(VI), Ni(II), Fe(II) and Cd(II) ions were 125.438, 112.397, 103.050 and 92.625 mg, respectively on the completion of the exhaustion time. It can be seen that the observed decrease in adsorption capacity was due to incomplete adsorption attributed to insufficient contact time of the aqueous phase in the fixed bed and the metal ions diffusion into the nanopores of MWCNTs-KIAGNPs⁴². Overall, lower flow rate favored Cr(VI), Ni(II), Fe(II) and Cd(II) ions adsorption owing to the higher uptake efficiency at lower flow rate. Previous studies have reported lower flow rate with a corresponding higher adsorption capacity^{47,79}.

Modelling of dynamic column. The prediction of the breakthrough curve for Cr(VI), Ni(II), Fe(II) and Cd(II) ions dynamic adsorption by MWCNTs-KIAGNPs surface was fitted using Thomas and Adams-Bohart model. Generally, Thomas model correlates with Langmuir isotherm and pseudo-second order kinetics assuming ideal model without axial diffusion, while Adams-Bohart model assumes non instantaneous balance where the rate of adsorption is dependent on remaining concentrations of metal ions and adsorption capacity of MWCNTs-KIAGNPs⁴⁷. The calculated parameters of Thomas and Adams-Bohart model are presented in Table 7. Comparison of the fitness of dynamic adsorption data with the models were based on the higher values of R^2 . Consequently, Table 7 shows that the experimental data were best fitted by Thomas model with R^2 above 0.964, compared to the Adams-Bohart model with the highest R^2 of 0.887, thereby corresponding to pseudo-second order rate driving force⁸⁰. Above all, the results obtained for the continuous adsorption corresponds to results of batch adsorption based on assumption of Thomas model for pseudo-second order kinetics which remarks that adsorption process was mass transfer controlled at the interface, not by chemical reaction⁴⁹. In addition, Table 7 reveals that the determined data (q_e) from Thomas model showed strong closeness to the experimental data (q_e). In all dynamic adsorption, the K_{TH} which describe the transfer rate of metal ions was enhanced by higher metal ions inlet concentration, higher flow rate and lower bed depth, indicating the dominance of the overall kinetics by the external mass transfer. More so, K_{TH} provided the following adsorption order Cr(VI) > Ni(II) > Fe(II) > Cd(II) which may be explained by the variations in the metallic ionic radii and physicochemical properties of metal ions⁸¹. Similarly, it can be seen that higher metal ions inlet concentration, higher flow rate and lower bed depth resulted to lower values of q_e and may be linked to the insufficient contact time between the metal ions and MWCNTs-KIAGNPs. Therefore, the adsorption efficiency of MWCNTs-KIAGNPs towards Cr(VI), Ni(II), Fe(II) and Cd(II) ions in dynamic column is optimally improved by lower inlet concentration, lower flow rate and higher bed depth.

Physico-chemical characteristics of the treated water. The investigation of the physico-chemical parameters metal ion analysis revealed the acidic nature of the chemical industry wastewater and high compositions of chromium, nickel, iron, cadmium, TDS, BOD, COD, nitrate, chloride, phosphate, fluoride and sulphate above the permissible standard concentrations recommended by US, Environmental Protection Agency and World Health Organization^{82,83}. As can be seen in Table 8, the adsorption of the wastewater by MWCNTs-KIAGNPs significantly reduced the pollution parameters to fall within the threshold concentrations of the standards.

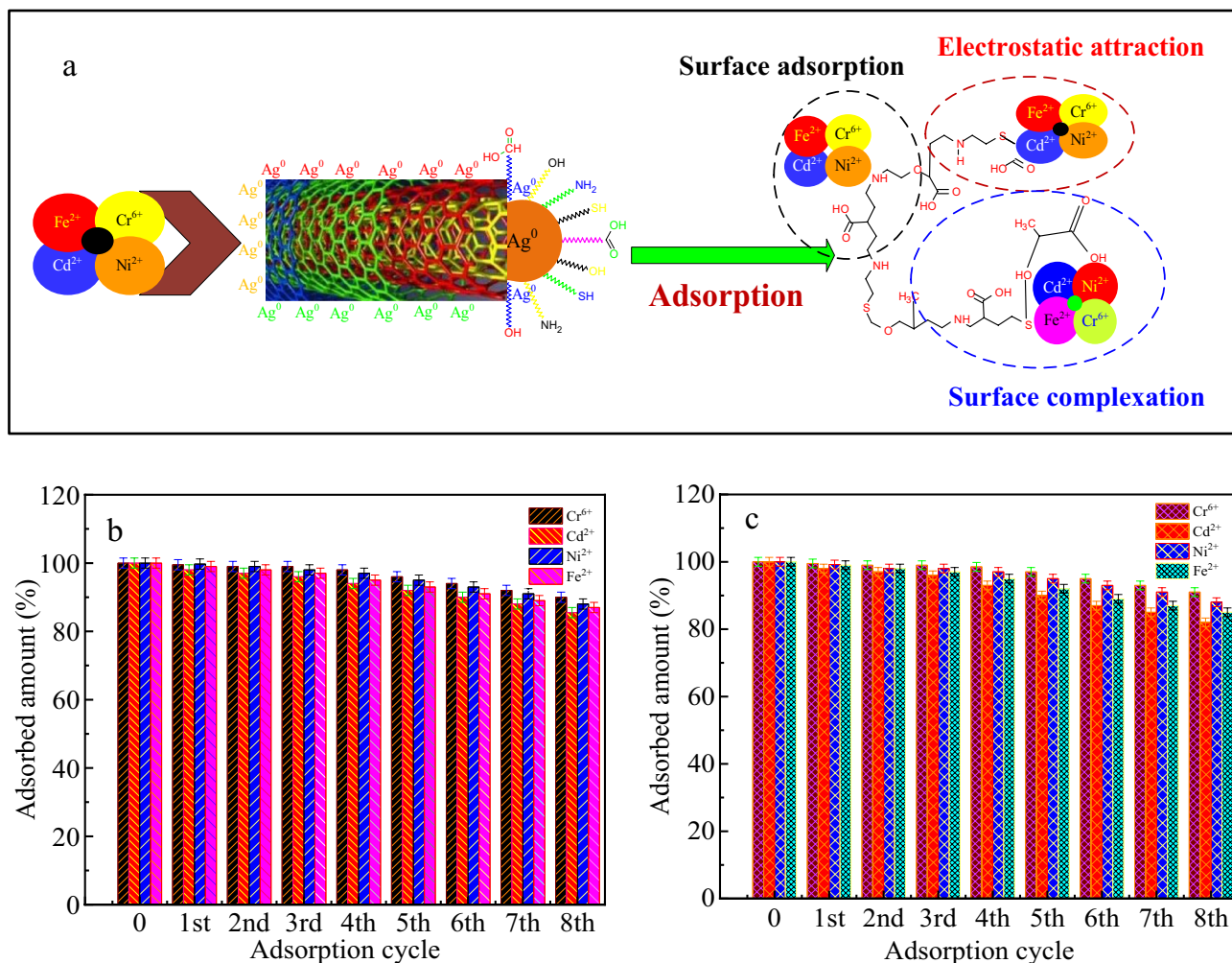


Figure 4. (a) possible adsorption mechanism of Cr(VI), Ni(II), Fe(II) and Cd(II) ions adsorption by MWCNTs-KIAGNPs; Reusability of MWCNTs-KIAGNPs towards Cr(VI), Ni(II), Fe(II) and Cd(II) ions adsorption in (b) batch system (MWCNTs-KIAGNPs dosage: 40 mg, pH 3 for Cr(VI) and 6 for Ni(II), Fe(II) and Cd(II) ions and contact time = 60 min) and (c) continuous system (bed depth = 6 cm, flow rate = 5 mL/min, influent concentration = Cr(VI) (21.25 mg/L), Ni(II) (16.50 mg/L), Fe(II) (14.00 mg/L) and Cd(II) (11.00 mg/L).

The observed reduction could be attributed to the attachment of the pollutants to the functional groups and massive adsorption sites of the nano adsorbent⁵⁰. In view of the results, the obtained treated water in both batch and column adsorption could be reused for various household and industrial purposes.

Adsorption mechanism. Through the analytical results of HRSEM (Fig. 1i) and FTIR (Fig. 2b) spectra, the possible mechanism of Cr(VI), Ni(II), Fe(II) and Cd(II) ions adsorption by MWCNTs-KIAGNPs shown in Fig. 4a was principally controlled simultaneously by supportive parameters including electrostatic interaction, surface adsorption and surface complexation. In view of the HRSEM information, the porous surface of MWCNTs-KIAGNPs enhanced the mass transfer and provided adsorption routes and area responsible for Cr(VI), Ni(II), Fe(II) and Cd(II) ions removal via diffusion to the pores and subsequent attachment to the surface of the adsorbent. However, the occurrence of electrostatic interaction was clearly evident between the positively charged metal (Cr(VI), Ni(II), Fe(II) and Cd(II)) ions and negatively charged MWCNTs-KIAGNPs adsorbent above the pH_{PZC} .

In addition, the monolayer adsorption indicated dominance of the adsorption process in both batch and continuous process, validated by the Langmuir isotherm and Thomas model. Also, ion exchange and surface complexation were obvious in the combination of the positively charged metal ions and the active sites of negatively charged MWCNTs-KIAGNPs through electrostatic attraction, and subsequent removal via the carboxyl and hydroxyl groups⁴².

Incidentally, the FTIR spectra of MWCNTs-KIAGNPs before and after adsorption of metal ions failed to reveal obvious change, except for the disappearance of adsorption peaks matching 704 (C-H) and 3890 cm^{-1} (NH₂, -NH- and -OH) after adsorption. This shows that the bonding of the metal ions with the hydroxyl groups were formed through surface complexation, whereas the hydroxyl/deprotonated groups could form complexes with

Cr(VI), Ni(II), Fe(II) and Cd(II). Hence, the surface complexation mechanism occurred via metal ions deposition on the adsorbent-adsorbate interface and intermolecular interaction between the metal ions and the adsorbent⁶⁶.

Batch/column reusability. To further affirm the viability and longevity of the multi-functional MWCNTs-KI AgNPs for wastewater treatment, reusability was examined through adsorption–desorption techniques to validate the economical sustainability of the adsorbent. It is noteworthy that Cr(VI), Ni(II), Fe(II) and Cd(II) ions were remarkably recuperated from MWCNTs-KI AgNPs, affirming the applicability of the adsorbent for at least 8 cycles as shown in Fig. 4b,c.

It can be seen that the total adsorption capacity after 8 adsorption cycles in batch mode were Cr(VI) (91%), Ni(II) (89%), Fe(II) (87%) and Cd(II) (85.5%), respectively. Similarly, the adsorption capacity in the continuous adsorption system were revealed as Cr(VI) (90%), Ni(II) (88%), Fe(II) (85%) and Cd(II) (82%), respectively after the 8th adsorption cycle. It is noteworthy in column regeneration that reduction in saturation time was observed via progression of the regeneration process from first to eight adsorption cycle, thereby resulting to reduce adsorption capacity and expanded mass transfer zone. Meanwhile, the decline in adsorption behavior of both batch and column process may be attributable to the protonation of the adsorption sites and weakening of continuously used functional groups. Apparently, the observed slight reduction in adsorption capacity may also be ascribed to the accumulation of metal ions in the stacked tubular structures hindering metal ions further access to the binding sites⁶⁵. Therefore, MWCNTs-KI AgNPs adsorbent possess excellent adsorption capacity, high selectivity and extended reusability capacity for efficient and economical recovery of metal ions from wastewater in both batch and column mode.

Conclusion

In summary, the synthesis of AgNPs demonstrated using *Khaya ivorensis* (KI) leaves extract for the fabrication of MWCNTs-KI AgNPs was reported for the first time and employed for the adsorption of Cr(VI), Ni(II), Fe(II) and Cd(II) ions from chemical industry wastewater in a static (batch) and dynamic (continuous) processes. In the batch adsorption study, maximum adsorption of metal ions by MWCNTs-KI AgNPs were recorded at adsorbent dosage (40 mg), pH (3 for Cr(VI) and 6 for Ni(II), Fe(II) and Cd(II) ions) and contact time (60 min). Based on the fitness of the experimental data, Langmuir isotherm and pseudo-second order kinetic model demonstrated the best fit, indicating a monolayer and chemisorption controlled process. Evidently, thermodynamic parameters revealed that the adsorption process was endothermic and spontaneous. Furthermore, fixed bed adsorption columns validated the effectiveness of metal ions adsorption by MWCNTs-KI AgNPs at various operational conditions of low influent concentration, low flow rate and high bed depth. Notably, the experimental data was nicely predicted by Thomas model, which showed corroboration with the Langmuir isotherm and pseudo-second order kinetics in batch mode. Remarkably, the batch/column reusability study demonstrated that the metal ions removal percentage were still over 80%, even after the 8th adsorption cycle. Overall, this study indicates the potentials of MWCNTs-KI AgNPs for wastewater treatment processes and may open novel approach towards developing robust nano sorbents for environmental remediation and related applications.

Received: 28 August 2020; Accepted: 19 November 2020

Published online: 08 January 2021

References

1. El-Tawil, R. S. *et al.* Silver/quartz nanocomposite as an adsorbent for removal of mercury (II) ions from aqueous solutions. *Heliyon* **5**, e02415 (2019).
2. Baby, R., Saifullah, B. & Hussein, M. Z. Palm kernel shell as an effective adsorbent for the treatment of heavy metal contaminated water. *Sci. Rep.* **9**, 1–11 (2019).
3. Abdul, S., Siva, A. T., Sankara, R., Muditana, R. & Lakshmi, K. V. D. Efficient and recyclable visible light-active nickel–phosphorus co-doped TiO₂ nanocatalysts for the abatement of methylene blue dye. *J. Nanostruct. Chem.* <https://doi.org/10.1007/s40097-020-00343-z> (2020).
4. Liu, Z., Li, X., Zhan, P., Hu, F. & Ye, X. Removal of cadmium and copper from water by a magnetic adsorbent of PFM: Adsorption performance and micro-structural morphology. *Sep. Purif. Technol.* **206**, 199–207 (2018).
5. Zhang, H. *et al.* Enhanced removal of heavy metal ions from aqueous solution using manganese dioxide-loaded biochar: Behavior and mechanism. *Sci. Rep.* **10**, 1–13 (2020).
6. Sangeetha, K., Vidhya, G. & Girija, E. K. Lead and cadmium removal from single and binary metal ion solution by novel hydroxyapatite/alginate/gelatin nanocomposites. *J. Environ. Chem. Eng.* <https://doi.org/10.1016/j.jece.2018.01.018> (2018).
7. Pradhan, S. K., Pareek, V., Panwar, J. & Gupta, S. Synthesis and characterization of ecofriendly silver nanoparticles combined with yttrium oxide (Ag–Y₂O₃) nanocomposite with assorted adsorption capacity for Cu(II) and Cr(VI) removal: A mechanism perspective. *J. Water Process Eng.* **32**, 100917 (2019).
8. Nawaz, T., Zulfiqar, S., Sarwar, M. I. & Iqbal, M. Synthesis of diglycolic acid functionalized core-shell silica coated Fe₃O₄ nanomaterials for magnetic extraction of Pb(II) and Cr(VI) ions. *Sci. Rep.* **10**, 1–13 (2020).
9. Xu, J. *et al.* A review of functionalized carbon nanotubes and graphene for heavy metal adsorption from water: Preparation, application, and mechanism. *Chemosphere* **195**, 351–364 (2018).
10. Jiang, D. *et al.* Removal of the heavy metal ion nickel (II) via an adsorption method using flower globular magnesium hydroxide. *J. Hazard. Mater.* **373**, 131–140 (2019).
11. Mustapha, S., Tijani, J. O., Ndamitso, M. M., Abdulkareem, S. A. & Shuaib, D. T. The role of kaolin and kaolin/ZnO nanoadsorbents in adsorption studies for tannery wastewater treatment. *Sci. Rep.* 1–22, <https://doi.org/10.1038/s41598-020-69808-z> (2020).
12. Muzaffar, S. & Tahir, H. Enhanced synthesis of silver nanoparticles by combination of plants extract and starch for the removal of cationic dye from simulated waste water using response surface methodology. *J. Mol. Liq.* **252**, 368–382 (2018).
13. Santhosh, C. *et al.* Removal of cationic and anionic heavy metals from water by 1D and 2D-carbon structures decorated with magnetic nanoparticles. *Sci. Rep.* **7**, 1–11 (2017).

14. Zheng, X. *et al.* Adsorption properties of granular activated carbon-supported titanium dioxide particles for dyes and copper ions. *Sci. Rep.* **8**, 3–11 (2018).
15. Haghhighizadeh, M., Zare, K., Aghaie, H. & Monajjemi, M. Preparation and characterization of Chicory leaf powder and its application as a nano-native plant sorbent for removal of Acid Blue 25 from aqueous media : Isotherm, kinetic and thermodynamic study of the adsorption phenomenon. *J. Nanostruct. Chem.* <https://doi.org/10.1007/s40097-019-00330-z> (2020).
16. Yang, J. *et al.* Nanomaterials for the removal of heavy metals from wastewater. *Nanomaterials* **9** (2019).
17. Abdel Maksoud, M. I. A. *et al.* Insight on water remediation application using magnetic nanomaterials and biosorbents. *Coord. Chem. Rev.* **403**, 213096 (2020).
18. Peng, Z. *et al.* Advances in the application, toxicity and degradation of carbon nanomaterials in environment: A review. *Environ. Int.* **134**, 105298 (2020).
19. Khandare, D. & Mukherjee, S. A review of metal oxide nanomaterials for fluoride decontamination from water environment. *Mater. Today Proc.* **18**, 1146–1155 (2019).
20. Jawed, A., Saxena, V. & Pandey, L. M. Engineered nanomaterials and their surface functionalization for the removal of heavy metals: A review. *J. Water Process Eng.* **33**, 101009 (2020).
21. Wadhawan, S., Jain, A., Nayyar, J. & Mehta, S. K. Role of nanomaterials as adsorbents in heavy metal ion removal from waste water: A review. *J. Water Process Eng.* **33**, 101038 (2020).
22. Gusain, R., Kumar, N. & Ray, S. S. Recent advances in carbon nanomaterial-based adsorbents for water purification. *Coord. Chem. Rev.* **405**, 213111 (2020).
23. Alagappan, P. N., Heimann, J., Morrow, L., Andreoli, E. & Barron, A. R. Easily regenerated readily deployable adsorbent for heavy metal removal from contaminated water. *Sci. Rep.* **7**, 1–7 (2017).
24. Wu, H. *et al.* Chromium ion removal from raw water by magnetic iron composites and *Shewanella oneidensis* MR-1. *Sci. Rep.* **9**, 1–16 (2019).
25. Pirsahab, M. *et al.* Optimization of photocatalytic degradation of methyl orange using immobilized scoria-Ni/TiO₂ nanoparticles. *J. Nanostruct. Chem.* <https://doi.org/10.1007/s40097-020-00337-x> (2020).
26. Hoyos-Palacio, L. M. *et al.* Compounds of carbon nanotubes decorated with silver nanoparticles via in-situ by chemical vapor deposition (CVD). *J. Mater. Res. Technol.* <https://doi.org/10.1016/j.jmrt.2019.09.062> 1–6 (2019).
27. Iqbal, A., Saeed, A., Kausar, A., Arshad, M. & Mahar, J. Synthesis and characterization of DGEBA composites reinforced with Cu/Ag modified carbon nanotubes. *Heliyon* **5**, e01733 (2019).
28. Kayalvizhi, S. *et al.* Eco-friendly cost-effective approach for synthesis of copper oxide nanoparticles for enhanced photocatalytic performance. *Optik (Stuttg.)* **202**, 163507 (2020).
29. Malinga, N. N. & Jarvis, A. L. L. Synthesis, characterization and magnetic properties of Ni, Co and FeCo nanoparticles on reduced graphene oxide for removal of Cr (VI). *J. Nanostruct. Chem.* **10**, 55–68 (2020).
30. Jasrotia, T., Chaudhary, S., Kaushik, A., Kumar, R. & Chaudhary, G. R. Green chemistry-assisted synthesis of biocompatible Ag, Cu, and Fe₂O₃ nanoparticles. *Mater. Today Chem.* **15**, 100214 (2020).
31. Odeniyi, M. A., Okumah, V. C., Adebayo-Tayo, B. C. & Odeniyi, O. A. Green synthesis and cream formulations of silver nanoparticles of *Nauclea latifolia* (African peach) fruit extracts and evaluation of antimicrobial and antioxidant activities. *Sustain. Chem. Pharm.* **15**, 100197 (2020).
32. Hamed, S. & Shojaosadati, S. A. Rapid and green synthesis of silver nanoparticles using Diospyros lotus extract: Evaluation of their biological and catalytic activities. *Polyhedron* **171**, 172–180 (2019).
33. Egbosuba, T. C. *et al.* Enhanced adsorption of As (V) and Mn (VII) from industrial wastewater using multi-walled carbon nanotubes and carboxylated multi-walled carbon nanotubes. *Chemosphere* **254**, 126780 (2020).
34. Adusei, S., Otchere, J. K., Oteng, P., Mensah, R. Q. & Tei-mensah, E. Heliyon phytochemical analysis, antioxidant and metal chelating capacity of *Tetrapleura tetraptera*. *Heliyon* **5**, e02762 (2019).
35. Kunatsa, Y., Chidewe, C. & Zvidzai, C. J. Phytochemical and anti-nutrient composite from selected marginalized Zimbabwean edible insects and vegetables. *J. Agric. Food Res.* **2**, 100027 (2020).
36. Bouabid, K., Lamchouri, F., Toufik, H., El, M. & Faouzi, A. Phytochemical investigation, in vitro and in vivo antioxidant properties of aqueous and organic extracts of toxic plant: *Atractylis gummifera* L. *J. Ethnopharmacol.* 112640 <https://doi.org/10.1016/j.jep.2020.112640> (2020).
37. Chand, K. *et al.* Green synthesis, characterization and photocatalytic application of silver. *Arab. J. Chem.* <https://doi.org/10.1016/j.arabjc.2020.01.009> (2020).
38. Moazzen, M. *et al.* Multi-walled carbon nanotubes modified with iron oxide and silver nanoparticles (MWCNT-Fe₃O₄/Ag) as a novel adsorbent for determining PAEs in carbonated soft drinks using magnetic SPE-GC/MS method. *Arab. J. Chem.* **12**, 476–488 (2019).
39. Chowdhary, P. *et al.* Bacterial degradation of distillery wastewater pollutants and their metabolites characterization and its toxicity evaluation by using *Caenorhabditis elegans* as terrestrial test models. *Chemosphere* 127689 <https://doi.org/10.1016/j.chemosphere.2020.127689> (2020).
40. Mutafela, R. N. *et al.* Radiometrical and physico-chemical characterisation of contaminated glass waste from a glass dump in Sweden. *Chemosphere* **241**, 124964 (2020).
41. Dehmani, Y. *et al.* Chemical characterization and adsorption of oil mill wastewater on Moroccan clay in order to be used in the agricultural field. *Heliyon* **6**, e03164 (2020).
42. Bo, S. *et al.* Efficiently selective adsorption of Pb(II) with functionalized alginate-based adsorbent in batch/column systems: Mechanism and application simulation. *J. Clean. Prod.* **250**, 119585 (2020).
43. Zhang, L., Niu, W., Sun, J. & Zhou, Q. Efficient removal of Cr(VI) from water by the uniform fiber ball loaded with polypyrrole: Static adsorption, dynamic adsorption and mechanism studies. *Chemosphere* **248**, 126102 (2020).
44. Langmuir, I. The adsorption of gases on plane surfaces of glass, mica and platinum. *J. Am. Chem. Soc.* **40**, 1361–1403 (1918).
45. Huang, J. *et al.* Enhancement of heavy metals removal by microbial flocculant produced by *Paenibacillus polymyxa* combined with an insufficient hydroxide precipitation. *Chem. Eng. J.* **374**, 880–894 (2019).
46. Lu, D. *et al.* Adsorption and desorption behaviors of antibiotic ciprofloxacin on functionalized spherical MCM-41 for water treatment. *J. Clean. Prod.* 121644, <https://doi.org/10.1016/j.jclepro.2020.121644> (2020).
47. Liu, Y. *et al.* Effective coating of crosslinked polyethyleneimine on elastic spongy monolith for highly efficient batch and continuous flow adsorption of Pb(II) and acidic red 18. *Chem. Eng. J.* 123610, <https://doi.org/10.1016/j.cej.2019.123610> (2019).
48. Zhang, Y., Jin, F., Shen, Z., Lynch, R. & Al-Tabbaa, A. Kinetic and equilibrium modelling of MTBE (methyl tert-butyl ether) adsorption on ZSM-5 zeolite: Batch and column studies. *J. Hazard. Mater.* **347**, 461–469 (2018).
49. Benjedim, S. *et al.* Removal of emerging pollutants present in water using an E-coli biofilm supported onto activated carbons prepared from argan wastes: Adsorption studies in batch and fixed bed. *Sci. Total Environ.* **720**, 137491 (2020).
50. Qu, J. *et al.* Multi-component adsorption of Pb(II), Cd(II) and Ni(II) onto microwave-functionalized cellulose: Kinetics, isotherms, thermodynamics, mechanisms and application for electroplating wastewater purification. *J. Hazard. Mater.* **387** (2020).
51. Dada, O. A. *et al.* Silver nanoparticle synthesis by *Acalypha wilkesiana* extract: Phytochemical screening, characterization, influence of operational parameters, and preliminary antibacterial testing. *Heliyon* **5**, e02517 (2019).
52. Tripathi, D., Modi, A., Narayan, G. & Rai, S. P. Green and cost effective synthesis of silver nanoparticles from endangered medicinal plant *Withania coagulans* and their potential biomedical properties. *Mater. Sci. Eng. C* **100**, 152–164 (2019).

53. Pereira, T., Lucia, V., Polez, P., Henrique, M. & Paulino, L. Modulating physical, chemical, and biological properties of silver nanoparticles obtained by green synthesis using different parts of the tree *Handroanthus heptaphyllus* (Vell.) Mattos. *Colloid Interface Sci. Commun.* **34**, 100224 (2020).
54. Siddiquee, M. A. *et al.* Green synthesis of silver nanoparticles from *Delonix regia* leaf extracts: In-vitro cytotoxicity and interaction studies with bovine serum albumin. *Mater. Chem. Phys.* **242**, 122493 (2020).
55. Ravichandran, V. *et al.* Green synthesis, characterization, antibacterial, antioxidant and photocatalytic activity of *Parkia speciosa* leaves extract mediated silver nanoparticles. *Results Phys.* **15**, 102565 (2019).
56. Yang, K. *et al.* Multiwalled carbon nanotubes incorporated with or without amino groups for aqueous Pb(II) removal: Comparison and mechanism study. *J. Mol. Liq.* **260**, 149–158 (2018).
57. Khosravi, R. *et al.* Chromium adsorption from aqueous solution using novel green nanocomposite: Adsorbent characterization, isotherm, kinetic and thermodynamic investigation. *J. Mol. Liq.* **256**, 163–174 (2018).
58. Mosaviniya, M. *et al.* Facile green synthesis of silver nanoparticles using Crocus Haussknechtii Bois bulb extract: Catalytic activity and antibacterial properties. *Colloids Interface Sci. Commun.* **33**, 100211 (2019).
59. Ahmad, N. *et al.* New magnetic silica-based hybrid organic-inorganic nanocomposite for the removal of lead(II) and nickel(II) ions from aqueous solutions. *Mater. Chem. Phys.* **226**, 73–81 (2019).
60. Trang, V. T. *et al.* Enhanced adsorption efficiency of inorganic chromium (VI) ions by using carbon-encapsulated hematite nanocubes. *J. Sci. Adv. Mater. Dev.* <https://doi.org/10.1016/j.jsamd.2020.05.007> (2020).
61. Aregay, G. G., Jawad, A., Du, Y., Shahzad, A. & Chen, Z. Efficient and selective removal of chromium (VI) by sulfide assembled hydroxalite compounds through concurrent reduction and adsorption processes. *J. Mol. Liq.* **294**, 111532 (2019).
62. Zhang, Y. *et al.* Recycling spent lithium-ion battery as adsorbents to remove aqueous heavy metals: Adsorption kinetics, isotherms, and regeneration assessment. *Resour. Conserv. Recycl.* **156**, 104688 (2020).
63. Dash, B., Dash, B. & Rath, S. S. A thorough understanding of the adsorption of Ni (II), Cd (II) and Zn (II) on goethite using experiments and molecular dynamics simulation. *Sep. Purif. Technol.* **240**, 116649 (2020).
64. Lazaratou, C. V., Panagiotaras, D., Panagopoulos, G., Pospíšil, M. & Papoulis, D. Ca treated Palygorskite and Halloysite clay minerals for Ferrous Iron (Fe²⁺) removal from water systems. *Environ. Technol. Innov.* **19**, 100961 (2020).
65. Ain, Q. U., Farooq, M. U. & Jalees, M. I. Application of magnetic graphene oxide for water purification: Heavy metals removal and disinfection. *J. Water Process Eng.* **33**, 101044 (2020).
66. Zhao, L. X. *et al.* Kinetic, thermodynamic and isotherm investigations of Cu²⁺ and Zn²⁺ adsorption on Li[sbnd]Al hydroxalite-like compound. *Sci. Total Environ.* **716** (2020).
67. Huang, X. *et al.* Competitive heavy metal adsorption onto new and aged polyethylene under various drinking water conditions. *J. Hazard. Mater.* **385**, 121585 (2020).
68. Sellaoui, L. *et al.* Understanding the adsorption of Pb²⁺, Hg²⁺ and Zn²⁺ from aqueous solution on a lignocellulosic biomass char using advanced statistical physics models and density functional theory simulations. *Chem. Eng. J.* **365**, 305–316 (2019).
69. Chen, Q., Zheng, J., Wen, L., Yang, C. & Zhang, L. A multi-functional-group modified cellulose for enhanced heavy metal cadmium adsorption: Performance and quantum chemical mechanism. *Chemosphere* **224**, 509–518 (2019).
70. Zhang, B. L. *et al.* Mechanism study about the adsorption of Pb(II) and Cd(II) with iron-trimesic metal-organic frameworks. *Chem. Eng. J.* **385**, 123507 (2020).
71. Egbosiuba, T. C. *et al.* Ultrasonic enhanced adsorption of methylene blue onto the optimized surface area of activated carbon: Adsorption isotherm, kinetics and thermodynamics. *Chem. Eng. Res. Des.* **153** (2020).
72. Kaveeshwar, Revellame, E. D., Gang, D. D., Zappi, E. & Subramaniam, R. Pecan shell based activated carbon for removal of iron (II) from fracking wastewater: Adsorption kinetics, isotherm and thermodynamic studies. *Process Saf. Environ. Prot.* 1–50, <https://doi.org/10.1016/j.psep.2017.12.007> (2018).
73. Kumar, P. & Chauhan, M. S. Adsorption of chromium (VI) from the synthetic aqueous solution using chemically modified dried water hyacinth roots. *J. Environ. Chem. Eng.* **7**, 103218 (2019).
74. Peng, G., Deng, S., Liu, F., Li, T. & Yu, G. Superhigh adsorption of nickel from electroplating wastewater by raw and calcined electroplating sludge waste. *J. Clean. Prod.* **246**, 118948 (2020).
75. Anitha, D., Ramadevi, A. & Seetharaman, R. Biosorptive removal of Nickel(II) from aqueous solution by Mangosteen shell activated carbon. *Mater. Today Proc.* **4**, 1–5 (2020).
76. Kocaoba, S. Adsorption of Fe(II) and Fe(III) from aqueous solution by using sepiolite: Speciation studies with MINEQL+ computer program. *Sep. Sci. Technol.* **55**, 896–906 (2020).
77. Shim, J., Kumar, M., Mukherjee, S. & Goswami, R. Sustainable removal of pernicious arsenic and cadmium by a novel composite of MnO₂ impregnated alginate beads: A cost-effective approach for wastewater treatment. *J. Environ. Manag.* **234**, 8–20 (2019).
78. Zhang, Y. *et al.* Adsorption of methyl tert-butyl ether (MTBE) onto ZSM-5 zeolite: Fixed-bed column tests, breakthrough curve modelling and regeneration. *Chemosphere* **220**, 422–431 (2019).
79. Hayati, B. *et al.* Heavy metal adsorption using PAMAM/CNT nanocomposite from aqueous solution in batch and continuous fixed bed systems. *Chem. Eng. J.* **346**, 258–270 (2018).
80. Ghasemi, S. S., Hadavifar, M., Maleki, B. & Mohammadnia, E. Adsorption of mercury ions from synthetic aqueous solution using polydopamine decorated SWCNTs. *J. Water Process Eng.* **32**, 100965 (2019).
81. Kharrazi, S. M., Mirghaffari, N., Dastgerdi, M. M. & Soleimani, M. A Novel Post-Modification of Powdered Activated Carbon Prepared from Lignocellulosic Waste Through Thermal Tension Treatment to Enhance the Porosity and Heavy Metals Adsorption. *Powder Technology* Vol. 366 (Elsevier B.V, 2020).
82. US EPA. *US Environmental Protection Agency: 2012 Edition of the Drinking Water Standards and Health Advisories. 2012 Edition Drinking Water Standards and Health Advisories.* EPA 822-S-12-001 2–6 (2012).
83. WHO. *Guidelines for Drinking-water Quality.* 4th Edn. 631, [https://doi.org/10.1016/S1462-0758\(00\)00006-6](https://doi.org/10.1016/S1462-0758(00)00006-6) (2017).

Acknowledgements

This work was financially supported by the Petroleum Technology Development Fund of Nigeria (grant number PTDF/ED/LSS/PhD/TCE/123/17).

Author contributions

T.C.E. designed the research work, conducted the experiments and wrote the main manuscript text. A.S.A., A.S.K. and E.A.A. supervised the present study. J.O.T., M.T.B. and S.B. contributed towards data analysis, editing and review of the manuscript. W.D.R. contributed towards the characterization of some of the samples. All authors read and approved the final manuscript.

Competing interests

The authors declare no competing interests.

Additional information

Supplementary Information The online version contains supplementary material available at <https://doi.org/10.1038/s41598-020-79857-z>.

Correspondence and requests for materials should be addressed to T.C.E.

Reprints and permissions information is available at www.nature.com/reprints.

Publisher's note Springer Nature remains neutral with regard to jurisdictional claims in published maps and institutional affiliations.



Open Access This article is licensed under a Creative Commons Attribution 4.0 International License, which permits use, sharing, adaptation, distribution and reproduction in any medium or format, as long as you give appropriate credit to the original author(s) and the source, provide a link to the Creative Commons licence, and indicate if changes were made. The images or other third party material in this article are included in the article's Creative Commons licence, unless indicated otherwise in a credit line to the material. If material is not included in the article's Creative Commons licence and your intended use is not permitted by statutory regulation or exceeds the permitted use, you will need to obtain permission directly from the copyright holder. To view a copy of this licence, visit <http://creativecommons.org/licenses/by/4.0/>.

© The Author(s) 2021